ISSN 1063-7729, Astronomy Reports, 2012, Vol. 56, No. 11, pp. 819–842. © Pleiades Publishing, Ltd., 2012.
Original Russian Text © I.B. Voloshina, T.S. Khruzina, 2012, published in Astronomicheskii Zhurnal, 2012, Vol. 89, No. 11, pp. 906–930.

Changes in the Parameters of the Accretion Disk around the Dwarf Nova SDSS J090350.73+330036.1 during an Outburst

I. B. Voloshina* **and T. S. Khruzina****

Sternberg Astronomical Institute, Lomonosov Moscow State University, Universitetskii pr. 13, Moscow, 119991 Russia

Received November 28, 2011; in final form, June 6, 2012

Abstract—R-band photometric light curves of the eruptive eclipsing binary SDSS J090350.73+330036.1 obtained during a superoutburst in May 2010 (JD 2455341–2455347) are analyzed. Observations covering an interval near the outburst maximum and the post-maximum decrease by 0.7^m are presented. Oscillations (superhumps) whose period differs from the orbital period by several percent are observed in the light curve together with eclipses, suggesting that the studied system is a SU UMa dwarf nova. A "spiral arm" model is used to fit the light curves and determine the parameters of the accretion disk and other components of the binary system. Together with a hot line, this model takes into account, geometrical inhomogeneities on the surface of the accretion disk, namely, two thickenings at its outer edge that decrease exponentially in the vertical direction with approach toward the white dwarf. The increase in the R-band flux from the system during the superoutburst mainly results from the enhanced luminosity of the accretion disk due to the increase in its radius by up to $\sim 0.44a_0$ at the outburst maximum (a_0 is the component separation), as well as a shallower radial temperature decrease law than in the canonical case. As the superoutburst faded, the disk radius decreased smoothly at the end of our observation (to $\sim 0.33a_0$), the thickness of its outer edge and temperature of its boundary layer decreased, and the parameter α_g approached its canonical value. Deviations from the mean brightness of the system as a function of the superhump period P_{sh} are analyzed for each out-of-eclipse set of observations. Various factors affecting the appearance and amplitudes of superhumps in the orbital light curves are considered.

DOI: 10.1134/S1063772912110078

1. INTRODUCTION

Eruptive variables (EVs) are close binary systems with short orbital periods and a wide range of parameters specifying the shapes of their light curves. Most close binaries in their final evolutionary stages are EVs. EVs generally consist of white-dwarf primaries that are gravitationally bound to late-type, evolved K–M secondaries that fill their Roche lobes. The EV evolutionary stage is characterized by a quasi-constant flow of matter from the secondary, which expands during its evolution and ejects its matter onto its nearby companion through the inner Lagrangian point L_1. An accretion disk that facilitates dissipation of the angular momentum of the inflowing matter forms around the white dwarf, provided that it has a sufficiently low magnetic field ($\leq 10^6$ G). The parameters of the accretion disks (size, temperature, luminosity, viscosity, etc.) vary over a wide range of acceptable values. Different sources can contribute appreciably to the total flux and determine the orbital variability, depending on the model: the secondary and associated ellipsoidal and reflection effects, an accretion disk with a complex shape (including possible geometrical perturbations of the inner surface of the disk), an optically thick part of the gas flow and the area where it interacts with the accretion disk (the so-called "hot line"), a shocked region on the windward side of the hot line and a hot spot on its leeward side, a boundary layer between the surface of the white dwarf and the inner layers of the disk, which specifies, for example, the disk luminosity, etc.

The main observed property of EVs is their outburst activity. Since eruptive activity and the scale of the observed phenomena are different for different systems, EVs are divided into several types: novae (a single large-amplitude outburst), recurrent novae (more than one outburst), dwarf novae (smaller, more frequent outbursts), and nova-like stars (with some characteristics similar to novae). The novae include classical and symbiotic novae. Dwarf novae are divided into three subclasses: U Gem, Z Cam, and SU UMa. SU UMa variables are characterized by the occurrence of superoutbursts, along with ordinary outbursts.

*E-mail: vib@sai.msu.ru
**E-mail: kts@sai.msu.ru

Normal outbursts in SU UMa stars are not prolonged, and are irregularly distributed in time. Many models have been proposed to describe these outbursts; see, e.g., [1]. These superoutbursts have much longer durations, and occur more rarely and have higher amplitudes (up to 4^m). The light curves of SU UMa stars always have superhumps with periods 3–7% longer than their orbital periods. The superoutburst profiles occurring in different systems of this type are similar: first, the brightness increases rapidly over ~10% of the total outburst duration T_0; after it reaches the maximum, the brightness decreases slowly over $\sim 0.8T_0$, with this latter stage being accompanied by the appearance of superhumps with amplitudes of $\sim 0.3^m$–0.4^m in the light curve, independent of the orbital inclination of the system. The brightness then falls rapidly to the pre-outburst level.

Many models have been proposed to describe the properties of superoutbursts and superhumps. Earlier models were based on possible asynchronous rotation of the donor star [2], the weak magnetic field of the white dwarf [3], elliptical orbits of binary components [4], variations in the rate of mass exchange [5, 6], instability of the accretion disk [7], and a combination of the two last models [8]. A review of these models, together with a discussion of their various shortcomings, can be found in [1].

The main factor characterizing a binary system is the shape of its light curve. The processes in accretion disks in their active state can be studied in detail using light curves of EVs during outbursts, since the nature of the stellar components of EVs is known fairly well (non-magnetic white dwarfs and normal stars), and their orbital variability can often be used to determine the geometry of the binary system reliably. By fitting the light curve of a close binary system using a specific model, we can determine the parameters of the stars, accretion disk, matter flows, and other components of the system, as well as estimate to what degree the model considered can plausibly explain observed features in the light curve.

The main goal of this paper is to verify whether or not a model with spiral arms representing geometrical inhomogeneities on the surface of accretion disk near its outer edge can be used to describe brightness variations observed in an SU UMa system during a superoutburst. We analyzed the poorly studied EV SDSS J090350.73+330036.1, which was discovered recently in the Sloan Digital Sky Survey (SDSS). We have determined the parameters of the binary system using detailed photometric observations during an outburst, and draw some conclusions about the applicability of the considered model. Section 2 presents currently available data on this variable system and Section 3 describes our own observations. Section 4 is devoted to the orbital ephemerides of SDSS J090350.73+330036.1 at the epoch of our observations. Light curves based on these ephemerides and the characteristic features of these light curves that specify the spiral-arm model used to determine the orbital parameters are considered in Section 5. The main parameters of the model are described in Section 6. Section 7 gives the results of out analysis of the system parameters during outburst and describes changes in these parameters during the brightness decline. Section 8 consideres factors that could affect the superhump parameters. The conclusions in Section 9 summarize the main results obtained in this paper.

2. BRIEF DESCRIPTION OF THE SYSTEM

The system SDSS J090350.73+330036.1 (further J0903) was identified as a new EV in the fourth year of the SDSS (2004–2005). J0903 was considered to be an eclipsing binary system with a high orbital inclination and an orbital period of ~1.3 h, based on the occurrence of brightness variations of $\Delta g \sim 1^m$ on time scales of 80–90 min [9]. SDSS monitoring of the object yielded several estimates of its brightness in the inactive state: $u = 18.89^m$, $g = 18.84^m$, $r = 18.79^m$ (the u, g, r filters have effective wavelengths of 3551, 4686, and 6166 Å, respectively, in the SDSS photometric system). We have for the red i and z filters $i = 18.87^m$ ($\lambda_{\rm eff} = 7480$ Å) and $z = 18.85^m$ ($\lambda_{\rm eff} = 8932$ Å) [9].

The eclipsing nature of J0903 was confirmed in [10]. Orbital ephemerides for this system were first determined using high time resolution photometric data obtained in the u, g, and r bands. Eleven eclipse epochs were used to analyze the light curve obtained on March 5–8, 2006, when the system was in its inactive state:

$$\text{Min. phot.} = \text{BJD } 2453800.394707 + 0.059073543^{\rm d} N.$$

Littlefair et al. [10] did not notice any appreciable deviations of the orbital period from a linear O–C relationship over the observation interval.

The main parameters of J0903 were derived by analyzing the shape and duration of the eclipse of the white dwarf, assuming that (1) the secondary fills completely its Roche lobe, i.e., $\mu = 1$, where μ is the Roche lobe filling factor, and (2) the eclipse width for the white dwarf depends only on the orbital inclination i and the component mass ratio q [10]. The radius of the white dwarf is derived from the duration of the eclipse ingress and egress (~40 s). A relationship between q and i can be obtained for a fixed eclipse semi-angle using the analytical expression for

Table 1. Parameters of SDSS J090350.73+330036.1 according to [10]

Parameter	Value	Parameter	Value
i, deg	80.8 ± 0.1	a_0, $R_\odot$	0.652 ± 0.006
$q = M_{wd}/M_{red}$	8.547 ± 0.220	K_{wd}, km/s	58 ± 2
M_{wd}, $M_\odot$	0.96 ± 0.03	K_{red}, km/s	494 ± 5
M_{red}, $M_\odot$	0.112 ± 0.004	R_d, a_0	0.27 ± 0.02
R_{wd}, $R_\odot$	0.0086 ± 0.0003	T_{wd}, K	13000 ± 300
R_{wd}, a_0	0.0132 ± 0.0006	d, pc	274 ± 10
R_{red}, $R_\odot$	0.141 ± 0.003		

a_0 is the distance between the centers of mass of the binary components, K_{wd} and K_{red} are the amplitudes of the radial-velocity curves of the white dwarf and the secondary, respectively, and d is the distance to the binary system.

a tangent to the Roche lobe. The disk radius R_d was calculated assuming that the gas flow direction corresponds to a ballistic trajectory and the hot spot is located at the point of intersection between the disk and this ballistic trajectory. The three unknown parameters (q, i, R_d) can be found using the times of ingresses and egresses of the hot-spot eclipses and the width of the white-dwarf eclipse. Finally, we assumed that the mass of the white dwarf corresponds to the theoretical mass–radius relationship for a white dwarf with the corresponding effective temperature, in order to determine the component masses using the obtained mass ratio q. In turn, the effective temperature was determined from the color changes that occur during the white-dwarf eclipse ingress and egress. This technique is valid only for observations with very high time resolution, and cannot be used if the time resolution is too low, so that the different eclipse stages cannot be clearly identified. Table 1 presents the parameters of J0903 obtained in [10].

The collection [11] of the fairly sparse data from the review [12] shows that the system was in an inactive state between September 2004 (MJD 2453250) and May 2010. The first information on the sharp increase in the brightness of J0903 by $\sim 4^m$, to $g \sim 14.6^m$–14.8^m, appeared after May 20, 2010 [13]. The first subsequent observations of this object (including ours) showed that the observed flux increase was actually due to a superoutburst, since the light curve displayed obvious superhumps [14].

This first detected J0903 superoutburst (BJD 2455341–2455352) after its discovery was observed by five teams of astronomers; the observational results are given in the review of Kato et al. [15], which is devoted to studies of a number of SU UMa systems during superoutbursts. Twenty five times of primary minima of J0903 were analyzed and the orbital ephemerides of the system were improved using the data of [10]

$$\text{Min. phot.} = \text{BJD } 2453800.394708(2) + 0.059073525(4)^{\text{d}} N. \quad (1)$$

The superhump ephemerides were also determined:

$$\text{Max. sh.} = \text{BJD } 2455340.4150 + 0.060320^{\text{d}} E. \quad (2)$$

The superhump period decreased from 0.060364^{d} to 0.060073^{d} during the outburst, at a rate of $\dot{P}/P \sim 12.3 \times 10^{-5}$.

3. OBSERVATIONS

The report of the detection of the superoutburst was received on May 23, 2010 (JD 2455340.3) [13, 14]. We began photometric observations of J0903 somewhat later due to the weather conditions, on May 24, when the system was already at its maximum brightness, and observed the object until May 30, 2010. Our observations were carried out during its slow decrease in brightness: the out-of-eclipse flux from the system decreased by 0.8^m over seven days. On average, the brightness decrease rate was 0.11^m/d, i.e., it took 8.8 days for the brightness to drop by 1^m, which corresponds to a mean value of $((9 \pm 1)^m/\text{d})$, as is characteristic of SU UMa systems [1].

The object was observed using an Apogee-47 CCD camera mounted on the 60-cm telescope of the Crimean Laboratory of the Sternberg Astronomical Institute. The durations of the observing runs depended on the weather conditions, and were normally 2 h. The observations were carried out in the R band of the Johnson photometric system, since our CCD receiver had its maximum sensitivity in the red.

Table 2. Journal of observations for SDSS J090350.73+330036.1 in 2010

Cycle number according to (1)	Start and end dates of the observations, JD 2455340+	Initial and final phases[1] $\varphi_1 - \varphi_2$	Observed epoch of minimum, JD 2455340+	Number of measurements n	$\Delta R_{\max}$	Eclipse depth, δR[3]
26085	$1.306^{\rm d}$–$1.376^{\rm d}$	0.636–0.815	–	39	$\sim 1.40^m$	–
26102	2.289–2.359	0.267–0.467	2.33424	62	1.70[2]	0.67^m
26119	3.312–3.391	0.591–0.928	3.33894	55	1.64	0.93
26136	4.291–4.380	0.174–0.677	4.34363	103	1.80	0.80
26152	5.260–5.312	0.573–0.446	5.28802	109	1.95	1.08
26169–26170	6.287–6.361	0.950–0.198	6.29259 6.35239	155	2.12	0.93
26186	7.297–7.356	0.046–0.042	7.29771	108	2.34	0.64

[1] The ephemerides (1) were used to calculate the initial φ_1 and final φ_2 observational phases.
[2] The maximum magnitude is given, beyond the anomalous maximum ($\Delta R_{\max} \sim 1.54^m$) detected at phases of $\varphi \sim 0.1$–0.15.
[3] The estimated eclipse depth is $\delta R = \Delta R_{\max} - \Delta R_{\min}$.

The star N139 near J0903 was used as a comparison star; several reference stars were used to monitor whether or not its brightness remained constant. We were not able to find reliable brightness estimates for this star. According to the NOMAD catalog [16], the brightness of N139 is $B = 14.180^m$, $V = 13.460^m$, $R = 13.350^m$. The catalog of positions and proper motions [17], which contains more than 18 million stars, gives the somewhat different estimates $B = 14.529^m$, $V = 13.889^m$, $R = 13.795^m$; i.e., uncertainties in the brightnesses of the comparison star are $\sim 0.4^m$, on average. Since there are no other stars with known brightnesses in the close vicinity of J0903, we give our R fluxes measured from the variable star in arbitrary units, i.e., $\Delta R = R_{J0903} - R_{\rm N139}$.

The observational data were processed using the aperture photometry method and the MAXIM-DL software package. Table 2 presents the details of the observations.

Figure 1 presents individual light curves of J0903 in May 2010, shown on the same scale. The light curves are presented in arbitrary units: the differences ΔR between the magnitudes of J0903 and the comparison star are plotted on the vertical axis, and the corresponding Julian Days are plotted on the horizontal axis. As the superoutburst proceeds, the shapes of the light curves change, and the superhumps evolve (Fig. 1). The observations on May 24, 2010 have large uncertainties due to bad weather, and are not presented here.

4. ORBITAL EPHEMERIDES

The ephemerides (1) used to determine the phases of our observations of J0903 yield systematic time shifts of the primary minima by phases of $\varphi \sim 0.04$–0.06. These phase shifts could have various origins: neglecting the barycentric correction to our observation epochs, insufficient time resolution of our observations, and distortions of the light-curve shape due to superhumps during the outburst.

The corresponding barycentric correction (BJD system) was introduced to the times t_i of our observations ($\sim 0.003^{\rm d}$, on average), and these times were used when calculating the orbital ephemerides of J0903 [15]. The use of the initial epoch of the BJD system yields a mean phase shift of $\Delta\varphi \sim 0.05$ when calculating the orbital phases obtained in the JD system; however, it is not correct to simply add $0.003^{\rm d}$ to the time of the initial epoch so as to use the ephemerides (1) for our observations, since the barycentric correction is time dependent. Therefore, we decided to use JD 2455342.33444, which is near the first observed primary minimum in our observations, as the initial epoch, and the value $P_{\rm orb} = 0.059073525^{\rm d}$ based on the ephemerides (1) as the orbital period. With regard to the chosen epoch of minimum, the light curve observed on May 25, 2010 has the number $N = 0$. Accordingly, the minimum observed on May 30, 2010 has the number $N = 84$.

Observations with high time resolution are required for precise determination of the epoch of the minimum, which corresponds to the middle of the eclipse of the white dwarf by the secondary. In this case, the epochs of eclipse ingresses and egresses

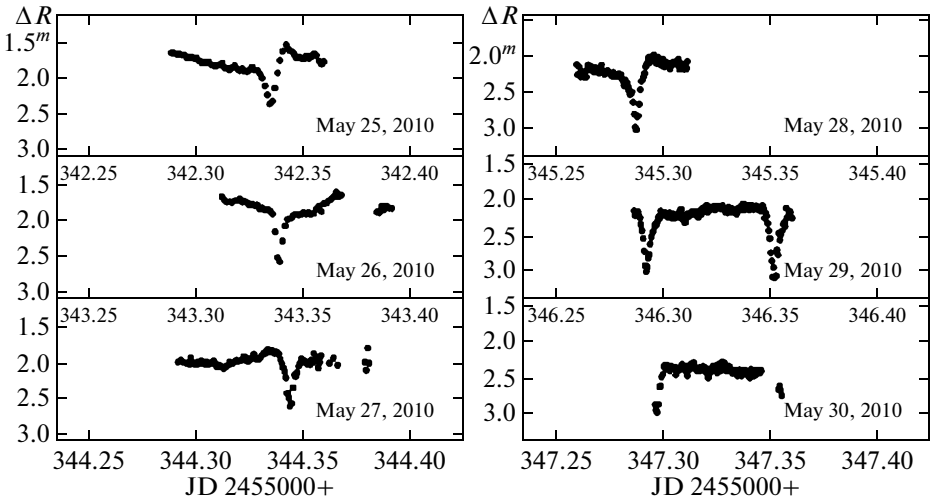

Fig. 1. Observed light curves of J0903 obtained on different dates during the superoutburst in May 2010 (JD 2455000.0+).

can be determined for the white dwarf, hot spot, and accretion disk using features in the light curve; accordingly, the mid-eclipse epoch of the white dwarf can be determined with good accuracy. The details of this procedure are described in [10, 18].

It is far more difficult to determine the mid-eclipse epoch for a white dwarf using low time-resolution observations, since it is not possible to reliably determine the epochs of the eclipse ingresses and egresses for the close-binary components; moreover, the observed minimum brightness does not necessarily correspond to the mid-eclipse of the white dwarf. Figure 2 shows eclipse curves for various close-binary components calculated using the parameters obtained for J0903 from the light-curve solution for cycle $N = 34$ (JD 2455344.3) of our observations. The bold curve (*0*) shows the observed minimum, where the points correspond to the phases of the measurements. The thin solid curves show the eclipse curves of the white dwarf (*1*), disk (*3*), and hot line (*4*); curve *2* indicates the change in the flux from the red dwarf due to the ellipsoidal effect. The vertical lines marked φ_1 and φ_2 indicate the eclipse ingress and egress phases for the white dwarf and the vertical dashed line w shows the mid-eclipse phase. The observed minimum brightness is the result of summing the fluxes from all the close-binary components (bold vertical line o), and is shifted relative to the eclipse of the white dwarf by $\Delta\varphi \sim 0.006$–0.008.

Figure 2 illustrates clearly that the time resolution of our observations (on average, 0.0005^{d} or $\sim 0.01P$) is insufficient to determine the mid-eclipse time for the white dwarf using the technique described in [18]. Therefore, we used the following algorithm to calculate the orbital phases for the light curves.

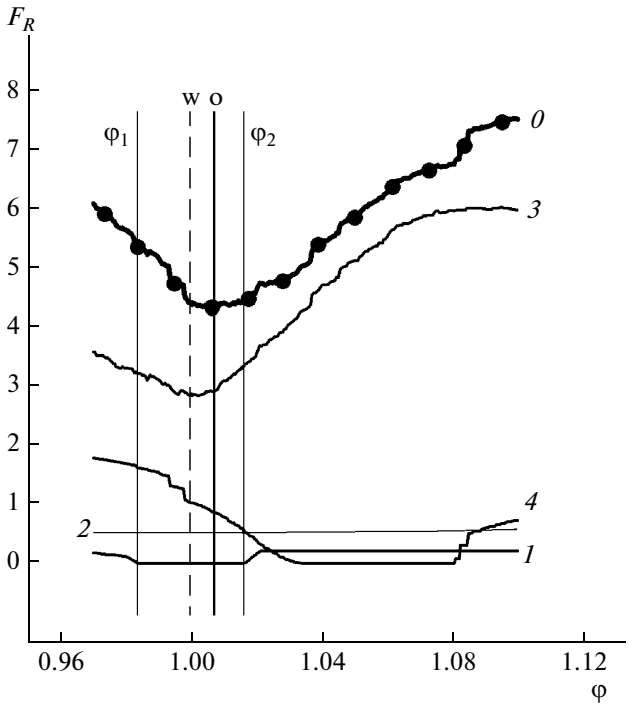

Fig. 2. Eclipse curves for the components of J0903 corresponding to the light-curve parameters of orbital cycle $N = 34$: curves *1*, *2*, and *3* show the eclipse curves for the white dwarf, the disk, and the hot line, respectively. Curve *2* shows how the flux from the red dwarf varies due to the ellipsoidal effect, and curve *0* is the total eclipse curve. The points in curve *0* denote the phases of measurements for the given observational set. Thin vertical lines φ_1 and φ_2 indicate the phases of eclipse ingress and egress for the white dwarf, the vertical dashed line (w) shows the mid-eclipse phase for the white dwarf, and the bold vertical line (o) denotes the phase of the minimum in the total eclipse curve.

Table 3. $O-C$ values for SDSS J090350.73+330036.1 during the superoutburst in May 2010 (see text)

N	Observed epochs of minima (O), JD 2450000+	Calculated epochs of minima (C), JD 2450000+	$O-C$, d
0	5342.33417	5342.33444	−0.00027
17	5343.33886	5343.33869	+0.00017
34	5344.34363	5344.34294	+0.00069
50	5345.28725	5345.28812	−0.00087
67	5346.29258	5346.29237	+0.00021
68	5346.35142	5346.35144	−0.00002
84	5347.29703	5347.29662	+0.00041

1. The ephemerides

$$\text{Min. phot.} = \text{JD } 2455342.33444 + 0.059073525^{\text{d}}N \quad (3)$$

were used to calculate the orbital phases at the observational epochs between May 24 and 30, 2010, and the corresponding mean light curves were constructed.

2. When determining the close-binary parameters based on the shape of the observed light curve, the array of fitted parameters was supplemented by $\Delta\varphi$—the orbital-phase shift of the observed relative to the model curve, such that the true mid-eclipse epoch for the white dwarf corresponds to phase $\varphi = 0.0$.

3. The calculated corrections were added to the phases of the normal points in the mean light curves (see Table 4), and also to the observed epochs of minimum brightnesses in Table 2.

Table 3 presents these improved epochs of minimum brightnesses derived from observations (O) and calculated using the ephemerides (3), as well as the $O-C$ deviations. Figure 3 shows the $O-C$ deviations as a function of the cycle number N. The solid line presents the mean value $O-C = 0.00004^{\text{d}}$. The local character of the observed deviations between $O-C$ and their mean value suggests that these deviations could be due to the effect of superhumps on the light curves.

5. LIGHT CURVES

Determination of the parameters of the system components using photometric data requires reliable light curves that have been cleaned of random fluctuations. Our data cover the outburst maximum (JD 2455341.3) and the subsequent drop in brightness (by $\sim 1^m$ for JD 2455347.3). For simplicity, light curve *1* will be taken to refer to the convolution of the observations for JD 2455341, light curve *2* to the observatons for JD 2455342, and so on, through JD 2455347 (light curve *7*).

Our light curves for J0903 show that the maximum flux from the system dropped by $\sim 0.8^m$ over seven days and the minimum flux decreased by $\sim 0.6^m$. The eclipse depth varied in the range 0.6^m–1.1^m during the outburst as the total brightness of the system decreased. Unfortunately, the observations carried out near the maximum of the superoutburst (May 24) are not sufficient to enable us to construct a complete light curve of the binary, since the data corresponding to eclipse phases are absent due to weather conditions. The observational runs obtained on successive nights contained one or two minima per run. The time resolution is 0.0005^{d}, on average, which corresponds to $\sim 0.01P$. According to [10], the eclipse duration for the white dwarf in J0903 is $\sim 0.04P$ in a spectral range close to the R filter, while the durations of eclipse ingress and egress are $\sim 0.008P$; therefore, there are between six and eight observational points corresponding to a complete eclipse, with our time resolution.

Figure 4 shows observational data obtained between JD 2455342 and JD 2455347 and convolved with the ephemerides (3). The individual (unaveraged) data reveal flux fluctuations at a level of $\sim 0.04^m$–0.12^m; the light curves obtained on May 28 (JD 2455345) and 30 (JD 2455347) have gaps of $\sim 0.13P$ and $\sim 0.14P$, respectively. Light curves *2* and *5* are anomalous; light curves *4* and *6*, with humps before eclipses, have close to classical curves; light curve *3* has a hump near an orbital phase of 0.5; and it is difficult to assign light curve *7* to some particular type, since the flux during the eclipse egress corresponds to the out-of-eclipse flux, and there is no hump before the eclipse ingress. Dips with different amplitudes at different orbital phases are visible in out-of-eclipse parts of all the light curves. Other EVs (e.g., UX UMa and IY UMa [19–21]) demonstrate similar patterns, both during outbursts and between their active and quiscent states.

Light curve *1* was obtained on May 24, 2010 (the first day of our observations; Fig. 5). This light curve cannot be used to reliably determine the close-binary parameters, since it does not include data corresponding to the eclipses of the white dwarf and the energy-release region. It can only be concluded that the mean R brightness of the system out of eclipse was $\Delta R \simeq 1.53(4)^m$ relative to the comparison star.

The mean light curves used to determine the parameters of J0903 are presented in Table 4. We did not average data within the primary minimum, to ensure that the shape of the minimum was not significantly distorted. To estimate the uncertainties

Table 4. Mean R light curves of J0903 during the superoutburst of May 2010

Curve *2* (JD 2455342) {62}				Curve *3* (JD 2455343) {55}				Curve *7* (JD 2455347) {108}			
φ	ΔR	σ	n	φ	ΔR	σ	n	φ	ΔR	σ	n
0.0172	2.331	0.013	1	0.0027	2.573	0.010	1	0.0090	2.952	0.013	1
0.0372	2.146	0.013	1	0.0227	2.285	0.010	1	0.0169	2.982	0.013	1
0.0572	1.935	0.013	1	0.0425	2.076	0.010	1	0.0251	2.875	0.013	1
0.0768	1.755	0.013	1	0.0758	1.976	0.008	2	0.0404	2.622	0.004	2
0.0968	1.633	0.013	1	0.1389	1.918	0.003	4	0.0566	2.468	0.017	2
0.1277	1.541	0.013	1	0.2283	1.900	0.004	5	0.0970	2.352	0.010	8
0.1573	1.622	0.010	2	0.3175	1.818	0.024	4	0.1697	2.381	0.010	10
0.2178	1.682	0.013	5	0.3870	1.726	0.015	3	0.2506	2.359	0.016	10
0.2694	1.700	0.014	5	0.4464	1.643	0.021	3	0.3152	2.353	0.016	6
0.3205	1.702	0.010	5	0.5163	1.654	0.013	2	0.3676	2.367	0.009	7
0.3685	1.708	0.018	5	0.5761	1.730	0.011	2	0.4200	2.436	0.014	6
0.4103	1.758	0.027	3	0.6157	1.743	0.006	2	0.4684	2.384	0.013	6
0.4432	1.778	0.008	3	0.6653	1.714	0.007	3	0.5330	2.352	0.014	10
0.5020	1.786	0.002	3	0.7248	1.741	0.004	3	0.5976	2.382	0.015	6
0.5614	1.829	0.004	3	0.7739	1.781	0.003	4	0.6420	2.425	0.015	5
0.6210	1.826	0.020	3	0.8101	1.813	0.016	3	0.6822	2.422	0.016	5
0.6804	1.874	0.010	3	0.8369	1.805	0.019	3	0.7266	2.434	0.018	6
0.7398	1.869	0.020	3	0.8696	1.827	0.002	3	0.7751	2.430	0.014	6
0.8092	1.897	0.010	4	0.9035	1.855	0.007	3	0.8194	2.409	0.007	5
0.8787	1.884	0.014	3	0.9432	1.909	0.010	1	0.9708	2.650	0.018	3
0.9181	1.944	0.013	1	0.9632	2.154	0.010	1	0.9768	2.753	0.013	1
0.9381	2.008	0.013	1	0.9830	2.517	0.010	1	0.9908	2.881	0.013	1
0.9581	2.115	0.013	1								
0.9777	2.241	0.013	1								
0.9976	2.367	0.013	1								

Curve *4* (JD 2455344) {103}				Curve *5* (JD 2455345) {109}				Curve *6* (JD 2455346) {155}			
φ	ΔR	σ	n	φ	ΔR	σ	n	φ	ΔR	σ	n
0.0064	2.599	0.015	1	0.0035	3.032	0.018	1	0.0013	3.003	0.047	3
0.0174	2.557	0.015	1	0.0156	2.843	0.007	2	0.0137	2.889	0.093	3
0.0284	2.341	0.015	1	0.0276	2.670	0.018	1	0.0256	2.705	0.043	3
0.0504	2.154	0.016	3	0.0357	2.470	0.018	1	0.0378	2.493	0.018	3
0.0781	2.018	0.017	2	0.0479	2.344	0.008	2	0.0479	2.511	0.063	2
0.1221	1.968	0.010	7	0.0600	2.289	0.018	1	0.0584	2.439	0.037	3
0.1692	1.989	0.009	6	0.0680	2.239	0.018	1	0.0686	2.351	0.025	2
0.2134	1.958	0.029	6	0.0762	2.148	0.018	1	0.0786	2.332	0.015	3
0.2423	1.966	0.025	4	0.0842	2.120	0.018	1	0.0890	2.318	0.065	2

Table 4. (Contd.)

Curve *4* (JD 2455344) {103}				Curve *5* (JD 2455345) {109}				Curve *6* (JD 2455346) {155}			
φ	ΔR	σ	n	φ	ΔR	σ	n	φ	ΔR	σ	n
0.2740	2.003	0.007	4	0.1004	2.060	0.024	3	0.1010	2.203	0.034	4
0.3223	1.983	0.007	6	0.1286	2.009	0.015	4	0.1214	2.197	0.010	6
0.3687	1.992	0.018	5	0.1569	2.048	0.030	3	0.1476	2.233	0.012	6
0.4233	2.006	0.017	4	0.1891	2.066	0.020	5	0.1916	2.232	0.012	6
0.4630	2.041	0.006	3	0.2295	2.091	0.016	5	0.2362	2.234	0.009	5
0.4959	2.047	0.011	3	0.2617	2.146	0.019	3	0.2766	2.222	0.031	5
0.5347	2.001	0.009	4	0.2860	2.105	0.010	3	0.3210	2.245	0.019	6
0.5786	1.973	0.007	4	0.3182	2.081	0.013	5	0.3695	2.191	0.007	6
0.6097	1.949	0.064	4	0.3505	2.131	0.026	3	0.4180	2.199	0.021	6
0.6391	1.939	0.021	4	0.3748	2.155	0.014	3	0.4665	2.126	0.012	6
0.6816	1.954	0.006	4	0.3989	2.141	0.033	3	0.5149	2.131	0.008	6
0.7255	1.915	0.016	4	0.5467	2.188	0.034	4	0.5645	2.117	0.004	6
0.7750	1.903	0.016	5	0.5750	2.257	0.021	3	0.6182	2.148	0.015	7
0.8246	1.832	0.012	4	0.5993	2.280	0.015	3	0.6706	2.155	0.010	6
0.8630	1.826	0.007	3	0.6236	2.170	0.024	3	0.7190	2.151	0.012	6
0.9017	1.855	0.005	4	0.6478	2.156	0.014	3	0.7675	2.113	0.013	6
0.9292	1.942	0.015	1	0.6720	2.178	0.021	3	0.8159	2.111	0.012	6
0.9402	1.991	0.015	1	0.7003	2.212	0.013	4	0.8643	2.127	0.011	6
0.9512	2.060	0.015	1	0.7327	2.192	0.024	4	0.9005	2.150	0.025	5
0.9621	2.109	0.015	1	0.7651	2.223	0.010	4	0.9165	2.177	0.023	3
0.9735	2.198	0.015	1	0.7935	2.240	0.003	3	0.9289	2.210	0.027	3
0.9845	2.415	0.015	1	0.8178	2.258	0.016	3	0.9387	2.237	0.025	2
0.9954	2.483	0.015	1	0.8421	2.283	0.002	3	0.9449	2.262	0.025	1
				0.8663	2.256	0.009	3	0.9491	2.334	0.025	1
				0.8945	2.335	0.032	4	0.9531	2.358	0.025	1
				0.9228	2.363	0.016	3	0.9589	2.441	0.025	2
				0.9429	2.457	0.030	2	0.9671	2.552	0.025	2
				0.9631	2.516	0.009	3	0.9754	2.741	0.012	2
				0.9792	2.640	0.018	1	0.9812	2.865	0.025	1
				0.9873	2.811	0.018	1	0.9853	2.928	0.025	1
				0.9953	2.997	0.018	1	0.9914	3.053	0.040	2

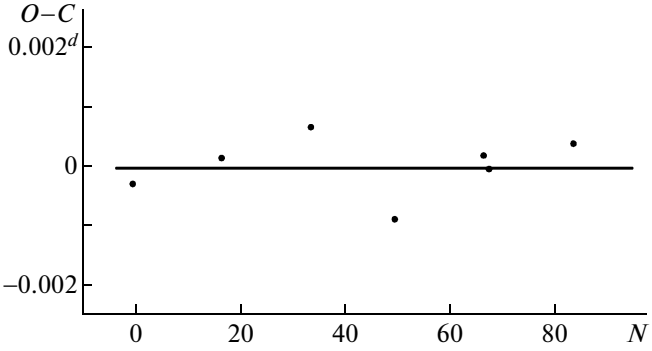

Fig. 3. $O-C$ as a function of the orbital cycle number N for J0903 during its outburst in May 2010.

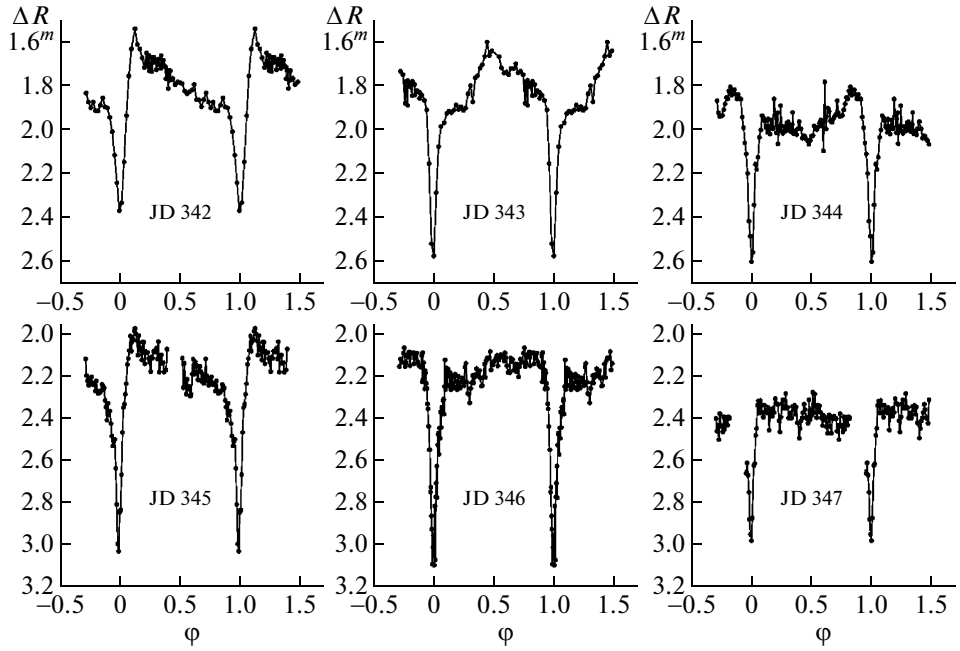

Fig. 4. Observed orbital curves of J0903 in the R band during the decline in brightness, near and after the superoutburst maximum. Phases based on the ephemerides (3) are plotted along the horizontal axis.

of these points, we used the mean σ calculated using a corresponding out-of-eclipse light curve. The total numbers of measurements in the considered observational datasets are given in curly brackets.

6. MODEL USED TO DETERMINE THE SYSTEM PARAMETERS

Spectroscopic observations of EVs (e.g., IP Peg, U Gem, EX Dra, SS Cyg, V347 Pup) during superoutbursts with high time resolution provide evidence for large-scale asymmetric features having the form of spiral arms located in the outer parts of accretion disks [22] and a shock in the form of "hot line" [23]. This spiral structure was first discovered in a study of the dwarf nova IP Peg during outburst [24].

The appearance of spiral arms is believed to be due to tidal shocks initiated by a fairly massive secondary [25] and changing conditions for angular-momentum transfer in the disk when the disk temperature increases during an outburst [26]. Three-dimensional gas-dynamical computations of flows of cool gas in close binaries [27] show that two spiral arms are formed in outer regions of the disk, with the orientation of the arms in a rotating reference system being almost constant. These computations also indicate that the appearance of a spiral-density wave in the inner (denser) layers of a slightly elliptical

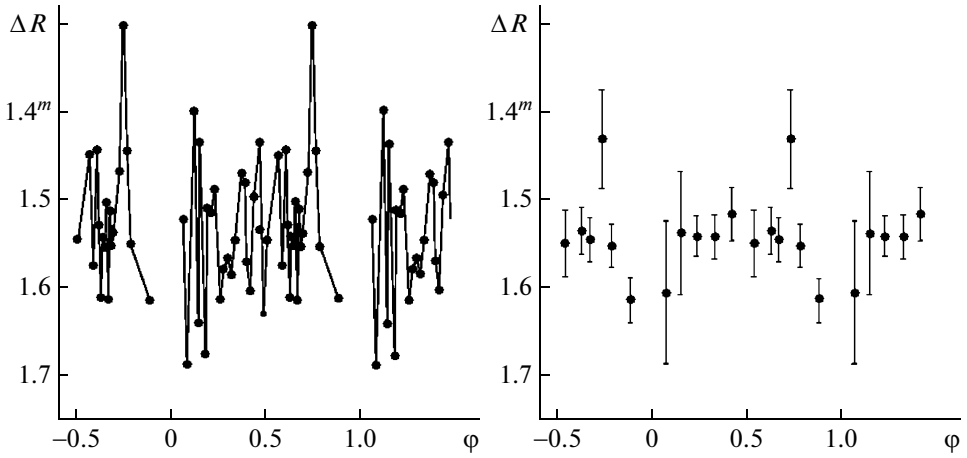

Fig. 5. The observed (left) and the mean (right) light curves of J0903 in the R band near the outburst maximum (JD 2455341).

disk, which precesses with a period that is a few percent greater than the orbital period, opposite to the direction of matter motion in the disk.

Spiral structure can be detected using both spectral and photometric observations of EVs if the spiral features protrude above the disk surface. Such spiral bulges were found on the accretion disk of the EV V1494 Aql (Nova Aql 1999-2) in a study of the photometric variability of this system [28]. Gas heating at the shock front and the increase in temperature and density inside the spiral arm lead to an increase in thickness of parts of the disk perpendicular to the orbital plane of the system. When these thickened parts of the outer edge of the disk lie in the line of sight, dips appear in the orbital light curve of the EV, due to the eclipse of inner, hotter regions of the disk [27, 29].

Dips can also arise in the light curves of close binaries when dense, massive blobs of matter in the outer parts of the disk are situated in the line of sight. These blobs can eclipse both the inner (hotter) parts of the disk and the white dwarf, if the velocities of the blobs differ from the velocity of the disk material [30]. This hypothesis was investigated in most detail in connection with the low-mass close-binary system HZ Her [30, 31]. The appearance of these blobs is believed to be due to a non-stationary outflow of matter from the secondary, in particular, the ejection of a massive blob of matter through the Lagrangian point L_1 toward the accretion disk. This blob interacts with the outer part of the disk and splits into a set of smaller clumps that move high above the orbital plane, resulting in dips in the observed light curves. Phenomenologically, these blobs resemble thickenings of the outer edge of the disk; since they move more slowly, they are not at rest in a coordinate system rotating with the orbital velocity. However, these blobs do not last very long (e.g., they survive for a few orbital periods in HZ Her).

In any case, whether they are spiral waves or blobs, these features are geometrical inhomogeneities protruding above the surface of the accretion disk, mostly near its outer edge, giving rise to eclipses of inner-disk regions.

Fitting the light curves of EVs in various activity states within various models [19–21] shows that the standard close-binary model with a hot spot in the region were a gaseous flow collides with the disk agrees well with a classical EV light curve, with a hump before the primary minimum, but fails completely to fit anomalous light curves and dips in light curves out of eclipse. The hot–line model [32] agrees well with observed anomalous light curves, e.g., humps during the egress from an eclipse, but it likewise cannot explain dips in light curves out of eclipse during outbursts. The best fit between the theoretical and observed light curves of EVs in their active states is achieved in models with geometrical inhomogeneities on the inner surface of the disk, near its outer edge [33]. Since the geometrical perturbations in this model have the form of spiral arms whose amplitudes decrease exponentially with approach toward the white dwarf, we they refer to them as "spiral arms". This model was used to determine the parameters of the J0903 components during the superoutburst.

The main aspects of our model used to explain the behavior of an eruptive variable during an outburst are listed below.

1. The surface of the secondary (red dwarf) is described using a Roche potential with a filling factor of $\mu = 1.0$. The stellar surface is described with 648 area elements, for each of which the radiation intensity toward the observer is calculated, taking

into account gravitational and edge darkening effects (using a non-linear edge-darkening law).

2. The surface of the primary (white dwarf) is approximated as a sphere of radius R_{wd}, whose center is located at one focus of the accretion disk.

3. The accretion disk is slightly elliptical (we specified $e = 0.05$ for this system). The unperturbed shape of the disk is described by a figure that is generated as follows:

—an ellipsoid with semi-axes a, b, and c is fitted to the outer surface of the disk, where a and b lie in the orbital plane and c is perpendicular to this plane;

—the inner surfaces of the disk are described by rotating paraboloids (for more detail see [34]);

—the orientation of the disk is determined by the angle α_e between the position vector drawn from the white-dwarf center to the disk periastron and the line connecting the centers of mass of the stars;

—the variation in the temperature is given by the relationship [35]

$$T(r) = T_{in}\left(\frac{R_{in}}{r}\right)^{\alpha_g}, \qquad (4)$$

where T_{in} is the temperature in the inner regions of the disk near the stellar equator, at a distance of $R_{in} \sim R_{wd}$ from its center. The parameter $\alpha_g = 0.75$ to first approximation, if every point of the surface radiates as a perfect blackbody [35]. In the active states of EVs, the flux from the disk increases by a factor of several hundred and α_g can decrease to $\sim$0.1 (see, e.g., [36]); as a result, the radial temperature distribution becomes flatter as the accretion-disk flux becomes higher. Both the radiative heating of an area element by the secondary (although this effect is not very important) and heating of this area by high-temperature radiation coming from inner regions of the disk are taken into account when calculating the local temperature of a given area element. This latter effect also leads to an increase in the temperature of the secondary surface facing its companion, that is, a reflection effect.

4. Simulations of the hot line and the associated parameters is described in detail in [32].

The hot line along the gaseous flow of matter emerging from the inner Lagrangian point L_1 is described as a part of an ellipsoid with semi-axes a_v, b_v, and c_v, which is elongated toward L_1. The lateral part of this ellipsoid coincides with the tangent to the elliptical disk, for any size and orientation of the disk, an the center of the ellipsoid is located in the orbital plane, in the disk at some distance ($\sim a_v$) from its edge. Only the part of the ellipsoid situated beyond the accretion disk is used as the hot line.

The energy of the shock is released at the hot line surface, in accordance with a Planck distribution, both at the shock front (on the side of the incident flux, or the "windward" side), and on the opposite ("leeward") side. The temperatures of area elements on the hot-line surface are calculated independently for each side. The temperature variation is determined by a cosine law with the maxima $T^{(1)}_{\max}$ and $T^{(2)}_{\max}$ on the windward and leeward sides, respectively. The minimum temperature of the hot line at the point $r_{\min}$ coincides with the temperature of matter located at a distance $r_{\min}$ from the center of mass of the white dwarf that is not heated by the shock.

5. The shapes and locations of the large-scale geometrical perturbations of the outer edge of the disk (the spiral arms) are described as two thickenings of the outer edge of the disk, on its inner surface, within a limited range of azimuth. The amplitudes of these spiral arms decrease exponentially toward inner parts of the disk. A detailed technique for constructing such a disk is given in [33].

In general terms, when simulating the geometrical perturbations on the surface of an elliptical disk, we assumed that, when the disk area with the coordanates (x, y, z) falls within a spiral arm, its z coordinate increases as

$$Z = z(x,y)h = z(x,y) \times \frac{\zeta}{\sqrt{[r/R_d(\psi) - \exp(\psi - \eta - B)]^2 + 0.0025}}. \qquad (5)$$

This formula defines a helical perturbation along the disk surface, explaining the name of the model. The coefficient ζ determines the wave amplitude, the angle ψ is the azimuth of the area (x, y, z) on the disk, and η is the angle between the periastron of the slightly elliptical disk and the position vector at which the spiral amplitude is maximum (the wave crest). The parameter B takes on values of 0 or 2π, depending on the area's position relative to the crest of the spiral arm. The second arm is located at position angles $\gamma + \eta > \psi > \eta$ (γ is the angular distance between the crests of the spiral waves, $\gamma \sim \pi$). The amplitude of the logarithmic spiral decreases very rapidly with approach toward the white dwarf; as a result, those parts of the spirals located in outer parts of the disk appreciably influence the observed flux from the disk. The temperatures of disk areas within the spiral arms increase by a constant value ΔT_{spir}, in accordance with the formula $T_{d,\,spir}(i) = T_d(i) + \Delta T_{spir}$.

Thus, this model enables us to determine the effect of outer-edge thickenings of the disk surface located within limited ranges of azimuth on the light curve of a close binary, and to estimate the depths and orbital phases of dips in the light curve, independent of the specific physical processes leading to the appearance of geometrical inhomogeneities on the disk surface. Although the code used was initially developed to fit

dips at orbital phases of ∼0.7 and ∼0.2, the azimuth of the spiral crest can be chosen arbitrarily.

Formally, the fitted parameters in this model are the component-mass ratio $q = M_{wd}/M_{red}$, orbital inclination i, effective temperatures of the white dwarf T_{wd} and red donor star T_{red}, radius of the white dwarf R_{wd}, and the temperature in inner regions of the disk (or at the boundary layer) near the white-dwarf equator T_{in}. The parameters of the slightly elliptical disk ($e = 0.05$) are the semi-major axis a, parameter α_g, which defines the radial temperature run in the disk in accordance with (4), azimuth of the disk periastron α_e, and thickness of the outer edge of the disk β_d. The parameters of the hot line are the ellipsoid semi-axes a_v, b_v, c_v, and the maximum temperatures of the matter heated by the shock at the surface of the line, near the outer edge of the disk, on the windward and leeward sides $T^{(1)}_{\max}$ and $T^{(2)}_{\max}$. These temperatures are added to the temperature $T_d(i)$ characterizing an area located at a distance $r(i)$ from the center of the disk when the shock is absent, according to (4): $T(i) = T_d(i) + T^{(n)}_{\max}\cos\delta r$, where $n = 1, 2$ and δr is the shift along the hot line. Considering the spiral arms introduces several new parameters: ζ, ΔT_{spir}, $\Delta_1 = \alpha_e - \eta$, and γ (or $\Delta_2 = 2\pi + \Delta_1 - \gamma$). The total number of parameters is 20 (in fact, the number of variables is 23, however, three are technical parameters that vary within a very narrow range, and variations of these parameters within these ranges affect the synthesized light curves only very slightly, compared to the effect of the main parameters). Thus, additional information on the system must be invoked in order to fix some parameters, in order to appreciably limit the variation ranges for the other parameters.

We fitted a set of homogeneous light curves of J0903 (obtained with the same equipment and the same comparison star), which differed mostly in their out-of-eclipse flux levels. This enabled us to impose an additional limit on the set of feasible parameters. Namely, given that there was a set of several light curves, we used the same energy unit to translate the synthesized light curves into magnitudes: the flux from the system at orbital phase $\varphi \sim 0.25$ in the light curve with the lowest out-of-eclipse brightness (curve *7*). This approach made it possible to use not only the shape but also the changing flux levels when fitting the synthesized to the observed light curves. This technique is described in detail in [20, 21, 37].

The Nelder–Mead method was used to search for the best-fit model parameters [38]. Some tens of different initial approximations were assigned for each light curve when searching for the global minimum of the residuals, since a set of local minima generally exist if there are numerous independent variables in a studied range of parameters. The quality of the fit between the theoretical and observed light curves in the chosen model was estimated using the residual

$$\chi^2 = \sum_{j=1}^{n} \frac{(m_j^{theor} - m_j^{obs})^2}{\sigma_j^2}, \qquad (6)$$

where m_j^{theor} and m_j^{obs} are the theoretical and observed magnitudes of the object at orbital phase j, σ_j^2 is the dispersion of the observations at orbital phase j, and n the number of normal points in the curve.

7. FITTING THE LIGHT CURVES DURING THE SUPEROUTBURST

We fitted the set of homogeneous light curves to determine the best-fit parameters of the system in the spiral-arm model in two stages. In the first, a normalized flux F_0 was determined to translate the theoretical values F into magnitudes and the ΔR_0 value corresponding to this flux. Curve *7* has the lowest out-of-eclipse brightness, and it should ideally have been used to normalize the set of homogeneous light curves; however, the low quality of this curve hindered us from being able to derive unambiguous parameters. Therefore, we obtained several different sets of best-fit parameters for this curve with almost identical minimum residuals. We first searched for fitted parameters independently with each of curves *2*–*7* without tying the to a unified flux scale. The parameters q, i, T_{wd}, and R_{wd} were limited to the ranges $q = 8.33$–8.77, $i = 80.7°$–$80.9°$, $R_{wd} = (0.0177$–$0.0196)\xi$, and $T_{wd} = 12\,700$–$13\,300$ K, in accordance with [10] (Table 1). The red dwarf temperature was varied in the range 2500–4000 K, and the disk radius in the range $(0.4$–$0.9)\xi$ (where ξ is the distance between the center of mass of the white dwarf and the inner Lagrangian point L_1; ξ is a function only of the component-mass ratio: $\xi = 0.7048a_0$ for $q = 8.547$).

For each of curves *2*–*7*, we chose the flux among our sets of solutions so as to satisfy all the light curves, namely, we took a flux of $F_0 = 5.425$ (in arbitrary units) to correspond to a relative magnitude of $\Delta R_0 = 2.36054^m$. The use of arbitrary units is due to the fact that the Planck function needed to calculate the fluxes from the area elements on the system components per unit wavelength interval (in our case, in cm) is the energy flux per unit area (per 1 cm^2). However, the unit for measuring distances in our software code is a_0, the distance between the close-binary components, which is *a priori* unknown.

In the second stage, the best-fit parameters for J0903 were searched for using light curves *2*–*7*, including the normalization of the fluxes to F_0. The following mean parameter values were fixed in order

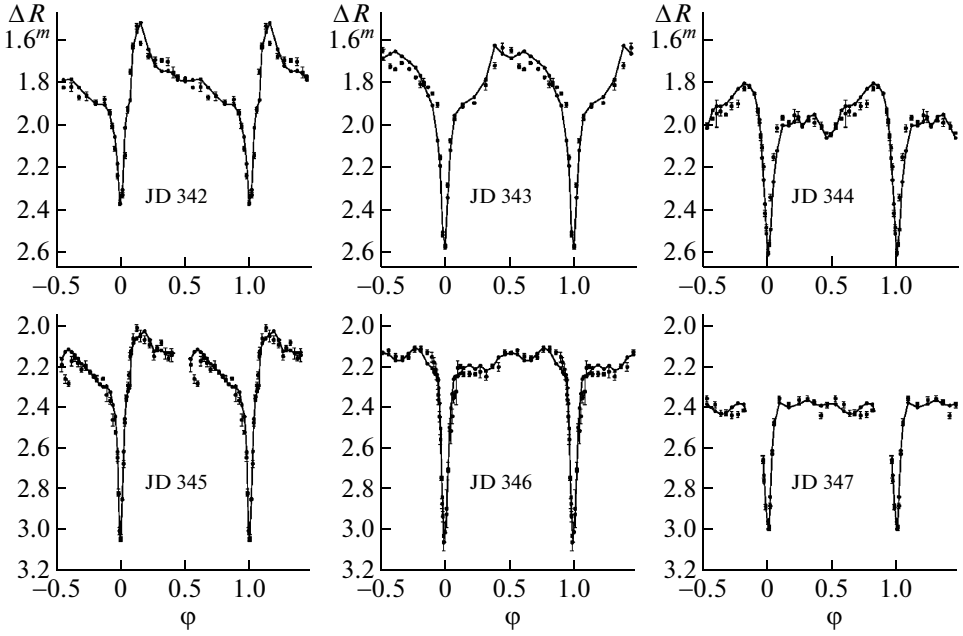

Fig. 6. Comparison of the mean light curves of J0903 (points) obtained during the May 2010 superoutburst with theoretical curves synthesized using the parameters in Table 5 (solid curves). The vertical bars indicate the rms uncertainties of the points in the mean curves.

to reduce the total number of unknown parameters: $q = 8.547$, $i = 80.8°$, $R_{wd} = 0.018715\xi = 0.0132a_0$, and $T_{wd} = 13\,000$ K [10]. The red-dwarf temperature was taken to be $T_{red} = 3325$ K. As was stated above, the eccentricity of the disk was taken to be $e = 0.05$ (for this eccentricity, the semi-minor axis of the disk is $b = 0.999a$, i.e., the disk is almost circular), and the normalization flux $F_0 = 5.425$ in arbitrary units corresponds to $\Delta R_0 = 2.36054^m$. The parameters of J0903 obtained from the fits for each of curves *2*–*7* are given in Table 5; Fig. 6 shows the theoretical light curves constructed with the corresponding parameters.

The spiral-arm model describes the geometrical perturbations on the surface of the accretion disk only schematically, since it ignores the fact that the three-dimensional gas-dynamical calculations of [29] suggest that these structures have different arm-crest amplitudes. Another disadvantage of the code used is the simplified structure of the area where energy is released due to the interaction between the gaseous flow and the accretion disk. Our code uses a simpler model for the hot line, whose lateral surface on the leeward side is located along the tangent to the disk surface; this choice was mostly due to our desire to reduce the number of unknown parameters in the problem. A cosine distribution of the temperature on this side of the hot line imitates a hot spot on the disk.

However, these disadvantages of the spiral-arm model do not prevent it from fitting the light curves of J0903 during its superoutburst in May 2010 fairly well (Fig. 6). These results enable us to conclude that the disk parameters change with the decreasing brightness of the system in our model.

The variations in the fluxes from the accretion disk and other components of the system during its superoutburst are shown in Fig. 7. A careful inspection of these plots show that the accretion disk contributes most to the flux of the system during its outburst: the maximum R flux from the disk achieved the maximum value of ∼8.1 units on the third observing night (JD 2455343); the maximum flux from the disk was slightly lower (∼7.7 units) on the previous night (JD 2455342), but a comparable contribution to the integrated flux was made by the windward side of the hot line (∼3.2 units), leading to the anomalously shaped light curve *2*. Therefore, the maximum out-of-eclipse flux in the mean light curves ($m_{\max}$ in Table 5) was estimated outside the radiating area of the windward side of the hot line, since we are considering changes occurring in the accretion disk. After the maximum, the flux from the disk decreased by one to two units per day, reaching ∼4.4–4.7 units on the final observing night.

The contributions of the red dwarf and hot line can be compared for curves *2* and *4*–*6*. The ellipsoidal variations in the flux from the red dwarf are distorted due to the reflection effect, i.e., heating of its surface by high-temperature radiation from the inner regions of the disk. The extent to which

Table 5. Parameters of the dwarf nova J0903 obtained from analysis of the system's light curve during its superoutburst in May 2010 in the spiral-arm model

Parameter	Curve *2* JD 2455342	Curve *3* JD 2455343	Curve *4* JD 2455344	Curve *5* JD 2455345	Curve *6* JD 2455346	Curve *7* JD 2455347
Cycle no. N	0	17	34	50	67–68	84
$m_{\max}$	1.7	1.64	1.80	1.95	2.12	2.34
$q = M_{wd}/M_{red}$	8.547 (fixed)					
i, deg	80.8 (fixed)					
T_{red}, K	3325 (fixed)					
$\langle R_{red}\rangle$, a_0	0.223 (fixed)					
R_{wd}	$0.018715\xi = 0.0132a_0$ (fixed)					
T_{wd}, K	13 000 (fixed)					
Parameters of the accretion disk						
e	0.05 (fixed)					
R_d/ξ(max)	0.643	0.655	0.630	0.608	0.495	0.494
R_d/a_0(max)	0.453	0.462	0.444	0.428	0.349	0.348
R_d/a_0(min)	0.410	0.418	0.402	0.388	0.316	0.315
a/a_0	0.431	0.440	0.423	0.408	0.333	0.332
T_{in}, K	37905	40598	38391	35757	30870	13116
$T_{d,out}$, K	3982	4163	3977	3738	3535	1544
β, deg	4.25	4.39	4.05	3.69	3.18	2.01
α_g	0.647	0.651	0.655	0.660	0.673	0.695
α_e, deg	124.9	110.1	124.9	115.1	129.8	130.1
Parameters of the hot line						
a_v/a_0	0.056	0.006	0.089	0.086	0.009	0.057
b_v/a_0	0.250	0.189	0.296	0.277	0.362	0.188
c_v/a_0	0.044	0.022	0.042	0.031	0.020	0.017
$T^{(1)}_{\max}$, K	34230	7713	19782	29051	8977	38754
$T^{(2)}_{\max}$, K	1243	4822	4656	718	3653	981
Parameters of the spiral waves						
ζ	0.184	0.370	0.300	0.187	0.447	0.488
ΔT_{spir}, K	3473	1937	1786	2649	3799	6889
$T_{d,\,spir}$, K	7455	6100	5763	6387	7334	8433
Δ_1, deg	115.3	7.0	175.6	105.7	6.6	21.4
Δ_2, deg	292.1	237.7	353.6	280.4	200.0	190.7
χ^2	550	1356	412	426	205	105

Δ_1 and Δ_2 are the angular distances between the spiral-wave crests and the line connecting the system components (measured clockwise from the disk periastron); $T_{d,\,out}$ is the mean temperature at the outer edge of the disk; $T_{d,\,spir} = \Delta T_{spir} + T_{d,\,out}$ is the temperature at the outer edge of the disk within the spiral.

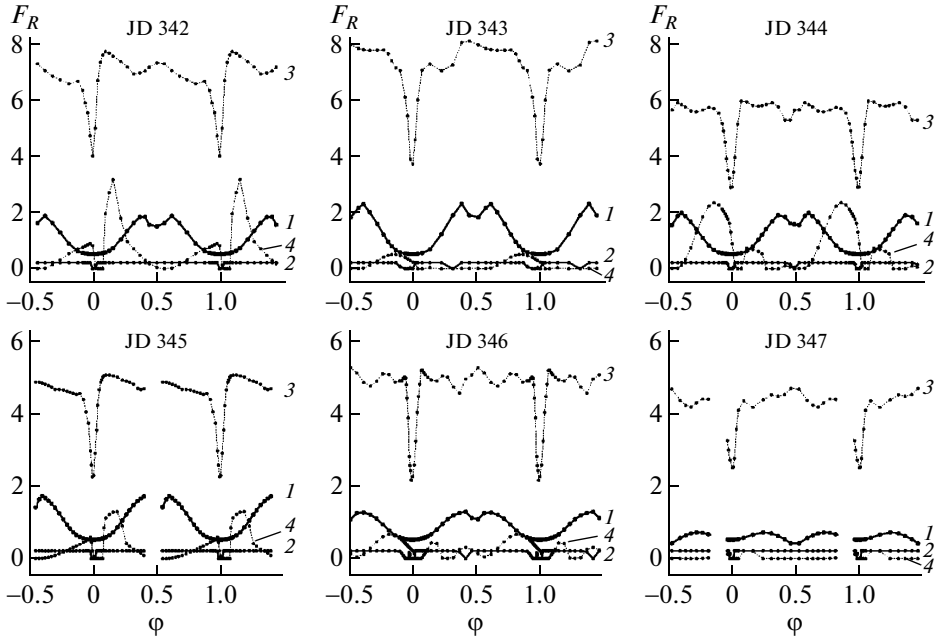

Fig. 7. Contributions of various components in J0903 to the integrated flux during the superoutburst (in arbitrary units): *1* red dwarf, *2* white dwarf, *3* accretion disk, *4* hot line.

the star is heated depends on the temperature T_{in}, which decreased smoothly during the outburst (Table 5) and approached the effective temperature of the white dwarf used in the calculations ($T_{wd} = 13\,000$ K) on the final observing night. Accordingly, the flux from the red dwarf decreases (both its maximum and mean values). The reflection effect was low on the final observing night (JD 2455347, Fig. 7) and ellipsoidal variations were mostly detected in the red-dwarf brightness.

The possibility of observing the flux from the windward side of the hot line depends strongly on the orientation of the slightly elliptical disk and the length of the region along the hot line where the shock radiates δr. Even for close values of δr, a change in the disk periastron azimuth can lead to either an eclipse of the shock region by the edge of the disk or to favorable conditions for its observation.

The flux from the white dwarf ($\sim$0.2 units) does not change during the superoutburst in our model; it is not high enough to be able to appreciably affect the light-curve shapes.

Thus, the phase-dependent radiation from an accretion disk with spiral arms is the major factor determining the dip phases and depths in this model; the hot line is manifest mostly through the amplitudes of the pre-eclipse and anomalous humps, while variations in the radiation from the secondary result in a small drop in the brightness near phase $\varphi \sim 0.5$, due to the integrated reflection and ellipsoidal effects in the red-dwarf brightness. The agreement between the synthesized and observed light curves for J0903 (Fig. 6) indicate a very satisfactory fit to the dip parameters in the spiral-arm model.

Let us consider how the model can explain the variability of the mean out-of-eclipse luminosity of the accretion disk averaged over an orbital cycle. Figure 8 shows the maximum out-of-eclipse flux $m_{\max}$ as a function of the orbital cycle number during the superoutburst, as well as some parameters of the accretion disk, such as its maximum ($R_{\max}$) and minimum ($R_{\min}$) radii, semi-major axis (a), temperature in inner regions (T_{in}), thickness of the outer edge of the disk in degrees β, and the dimensionless coefficient α_g, which determines the radial temperature distribution in the disk according to (4). The flux from the white dwarf does not vary, because its effective temperature was taken to be fixed in at the value 13 000 K; on the other hand, the superoutburst maximum is associated with an appreciable increase in the radiation intensity from the inner disk regions, that is, the boundary layer located near the stellar equator, which is a source of accreting matter onto the white dwarf, according to modern theory. Here, the temperature reaches a value of $T_{in} \sim 41\,000$ K at the outburst maximum and decreases to $\sim$13 000 K at the end of our observation. Figure 8 indicates that the increase in T_{in} at the superoutburst maximum (JD 2455343) is associated with an increase in the radius of the disk (R_d) and the thickness of its outer edge β. The mean disk radius

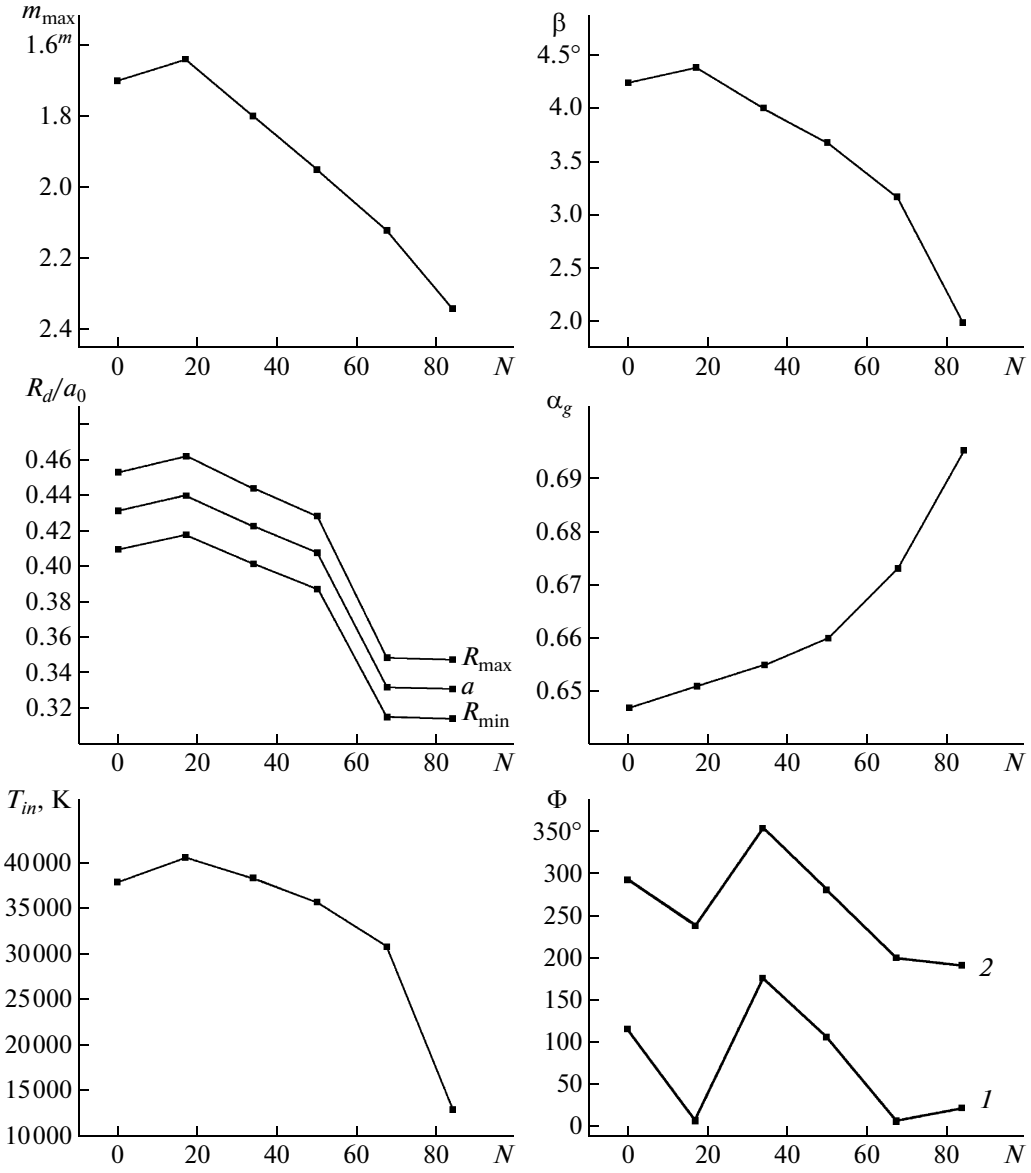

Fig. 8. Maximum out-of-eclipse flux m_{max} for the system and some disk parameters as functions of the orbital cycle number N (see the text).

near the outburst maximum reaches $a \sim 0.44a_0$ (or $a \sim 0.63\xi$, where ξ is the distance between the center of mass of the white dwarf and L_1). The drop in brightness by $\sim 0.7^m$ is accompanied by a decrease in the disk radius to $\sim 0.33a_0$ (or $a \sim 0.47\xi$), which is still 20% greater than its radius in the quiescent state: $R_d \sim 0.27a_0$ [10]. We conclude that the object was still undergoing the stage of a slow decrease in brightness, and had not achieved its pre-outburst state on the final observing night.

However, if the contributions from the other components are small, the increase in the disk radius alone cannot provide the luminosity observed at the maximum of the superoutburst. Not only the size of the disk but also the character of the radial temperature distribution affects the flux from the disk. In our model (see Section 6), this distribution is determined by (4); i.e., the values of T_{in} in the boundary layer and α_g. For $\alpha_g = 0.75$, each area element is in radiative equilibrium, i.e., every point on the surface of the disk radiates as an perfect blackbody; the smaller the value of α_g, the shallower the temperature distribution over the disk and the higher its luminosity. α_g was minimum ($\alpha_g = 0.647$) for light curve *2*. The radial temperature distribution smoothly approached the equilibrium on subsequent days as the brightness

was falling off after the maximum and α_g approached its canonical value of $\alpha_g = 0.75$.

We emphasize that our conclusions that there was an increase in the temperature in the inner disk and growth of the disk radius during the outburst, and a smooth recovery of the balance between the release of gravitational energy and radiative cooling (i.e, approach of α_g to its canonical value of 0.75) as the system was returning to its quiescent state, are based on the R light curves. The increase in temperature in the inner parts of the disk during the superoutburst shifts the radiation maximum toward shorter wavelengths; i.e., in general, the changes in the shapes of the light curves and the flux levels should have been more substantial in U, B, and V than in the red, where we observed. Multicolor light curves of high quality in the transition stages between quiescent states to outburst maxima and back are required to confirm our results and construct a more detailed picture of the evolution of the J0903 superoutburst. Unfortunately, it is fairly difficult to make these observations, since the initial increase in the brightness to the maximum (i.e., the very beginning of an outburst) occurs very rapidly in dwarf novae, and are usually observed only sporadically. High-quality light curves on the falling branches of outbursts in the U, B, and V filters can be obtained for faint objects ($\sim 14^m$–15^m) only with large telescopes. The integration times for our equipment when we observed J0903 during its superoutburst were ~100, ~150, and ~200 s in the V, B, and U filters, respectively, whereas the eclipse duration did not exceed ~205 s. Only one or two points fall into the eclipse region, which limits the information carried by light curves, even in V. In R, only ~40 s exposures were sufficient to estimate the brightness reliably, yielding four to six points to cover the eclipse region of the white dwarf and disk.

8. SUPERHUMPS AS OBSERVATIONAL MANIFESTATIONS OF GEOMETRICAL PERTURBATIONS AT THE OUTER EDGE OF THE DISK

Our observations of J0903 during the outburst clearly indicate the presence of superhumps in the light curves, suggesting it is an SU UMa variable. The main properties of these variables are described in detail in [1].

First, a superhump is always present in a light curve observed during a superoutburst. The superhump period P_{sh} is 3–7% longer than the orbital period, and generally decreases by 1–1.25% as the superoutburst evolves [39]. The superhump amplitude at the maximum brightness is $\sim 0.3^m$–0.4^m in the optical. As the superoutburst evolves, the superhump amplitude decreases more rapidly than the brightness falls off; the superhump profile broadens, and other features appear between the main humps [1, 40, 41].

Second, the appearance of superhumps does not depend on the orbital inclination of the system. Moreover, recurrent dips are present in eclipsing systems during superoutbursts, which are most clearly seen near phases of 0.25 and 0.75 [42]. Similar dips have been observed in the X-ray light curves of low-massive close binaries [43], and are explained by an increase in the vertical thickness of the edge of the disk (by up to 10° at the corresponding phases, to provide the observed depths of the dips in the UV [44]). Such dips are absent during ordinary outbursts.

Third, multicolor photometry of superhumps indicates that the superhump radiation becomes bluer at their minima and redder at their maxima. This tendency becomes stronger toward shorter wavelengths [45], and can be explained by re-radiation of the superhump flux: studies of UV dips in the Z Cha and OY Car systems observed during superoutbursts show that the increase in the vertical thickness of the disk near its outer edge leads to an eclipse of the center of the disk; the UV flux is partially absorbed and this flux is then re-radiated at longer wavelengths, enhancing the optical and IR radiation [46, 47].

Fourth, shifts of the γ velocities have been detected for wide absorption lines during superoutbursts; analysis of these line profiles shows that γ-velocity variations are due to changes in asymmetric features in the disk, rather than total line shifts [48]: many lines appear in the outer parts of the disk, which display non-circular motions. A feature that displays non-circular motion rotates with the period P_{sh} rather than the orbital period, which suggests that it is closely related to the source of superhump light. Eclipse ingresses and egresses are not accompanied by rapid intensity changes, suggesting that the superhump light source is an extended region on the disk spanning almost one-fourth of its surface [49].

The eclipse-mapping method used in numerous papers was effective in revealing the sources of superhump light and identifying three regions of the acrretion disk, from where radiation arrives: one located near the inner Lagrangian point L_1 and two others positioned symmetrically at the edge of the disk near phases $\varphi \sim 0.75$ and 0.25 [23, 50].

Numerous models have tried to explain the observational facts listed above (see Introduction). The best fits are achieved in models in which matter flows from a donor star and accumulates in the disk, leading to a gradual increase in the disk radius to $\sim 0.48a_0$ (for $q > 4.5$ and a non-viscous disk); the orbits of particles become unstable above this radius, and enhanced energy release occurs in areas of orbit intersections. A precessing elliptical ring forms at the

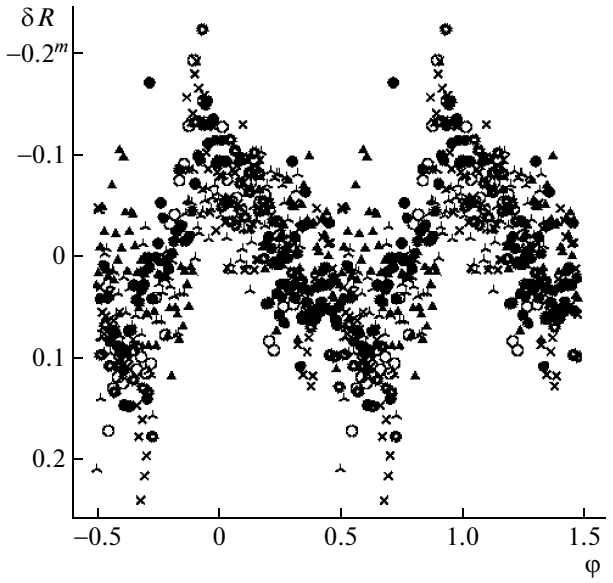

Fig. 9. Relative out-of-eclipse flux δR as a function of the phase ϕ of the superhump period P_{sh}.

outer edge of the disk [50, 51], where these areas of enhanced energy release are transferred along the edge of the disk due to Keplerian rotation.

An alternative mechanism for superhump formation in SU UMa stars was proposed in [27]. Its main points are as follows: (1) an accretion disk forms in a system between superoutbursts and accumulates mass until it becomes denser than the matter flowing from the inner Lagrangian point L_1; (2) inner parts of the disk cease to experience gas-dynamical perturbations, and a precessing spiral-density wave forms here; (3) this leads to an appreciable (by an order of magnitude) increase in the accretion rate, resulting in a superoutburst; (4) retrograde precession of the density wave and the compactness of the central region of energy release cause the appearance of superhumps with much longer periods P_{sh} than the orbital periods and independence of the orbital inclination. This mechanism seems to be able to explain the whole variety of observational data in SU UMa stars [27]; however, the eclipse-mapping method is not able to reveal the compact area with excess energy release on the surface of the accretor. This may be because this method is very sensitive to the linear sizes of features and cannot detect bright spots with such small areas as the surface of the accretor [27].

Our analysis using the geometrical spiral-arm model to determine the disk parameters during a superoutburst yielded results consistent with those obtained with the eclipse-mapping method (see Section 6): the hot line and spiral arms in the outer parts of the disk intersect the flux from the inner parts of the disk, appreciably influencing the light curve shapes during the J0903 superoutburst.

Let us consider the results obtained in the pure geometrical spiral-arm model we have used to determine the parameters of the disk and hot line during the evolution of the superoutburst in this system.

The previous section discussed in detail the clear decrease in the radius and thickness of the disk and the boundary-layer temperature (Fig. 8), as well as the growth of stability that occurred as the total out-of-eclipse brightness of the system was falling off.

Figure 8 also shows the change in the wave-crest azimuths $\Phi = \Delta_n$ ($n = 1, 2$) in degrees as a function of the orbital cycle number. All the variations of the crest azimuths during the outburst are similar, although the angular distance between wave crests shifts slightly from π on either side. The superhump period was determined in [15]: $P_{sh} = 0.060320^{\rm d}$. This is a beat period between the orbital period and the "precession" period P_{long}: $P_{sh}^{-1} = P_{\rm orb}^{-1} - P_{long}^{-1}$. The superhump light source makes one complete revolution in the rotating reference system over $P_{long} \sim 2.88$ days, that is $48.75 P_{\rm orb}$. This superhump light source made $\sim$1.7 revolutions in the rotating reference system during our observations. On the final observing night, the shift of the crest azimuths deviated from the correlation $\Phi(N)$ observed earlier. However, the small number of data points (only six points over 84 orbital cycles with a step of $\Delta N = 17$–18) hinder unambiguous conclusions about how the superhump light source moves as the activity of the system decays.

The other parameters of the spirals, namely, the crest height ζ and the temperature inside the spirals $T_{d,\,spir}$ (Table 5), describe the structure of the spirals fairly schematically; the number of unknowns will increase drastically if we try to describe the process in more detail. The parameter ΔT_{spir} for estimating the degree to which the disk matter is perturbed appreciably influences the parameters of the disk only at its outer edge, where it is comparable with the temperature of the unperturbed disk (Table 5); the effect of this parameter is substantially less in the inner regions of the disk. The temperature in the spirals $T_{d,\,spir} = \Delta T_{spir} + T_{d,\,out}$ changed smoothly near the outer edge of the disk as the outburst decayed (Table 5), reaching its maximum on the final observing night; however, there is no evidence for a clear correlation between changes in $T_{d,\,spir}$ and the disk parameters considered above.

Thus, we used the spiral-arm model to calculate light-curve parameters for J0903 on the descending branch of the outburst; in this model, we can unambiguously conclude that the azimuths of the spiral wave crests change when the outburst decays. This

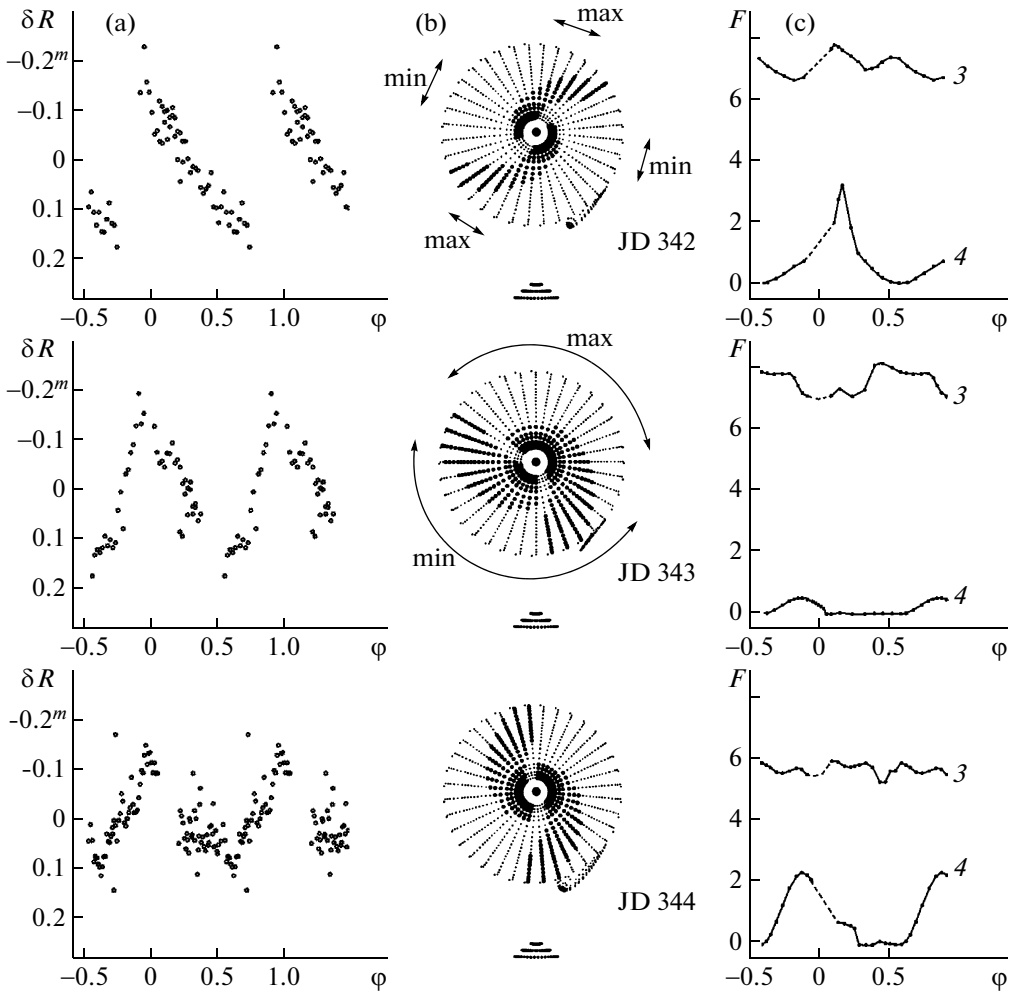

Fig. 10. (a) Relative out-of-eclipse brightness of J0903 as a function of the phase of the superhump period on different observing nights during the superoutburst in May 2010. (b) Orientation of spiral arms on the surface of the accretion disk; the arrows indicate regions of orbital phases with the maximum and minimum fluxes from the spiral arms on the disk (see text). (c) Contributions of the disk radiation (curves *3*) and the hot line (curves *4*) to the total out-of-eclipse flux. The curves correspond to observations obtained on May 25–27, 2010 (JD 2455342–JD 2455344).

conclusion does not depend on the physical reasons for the appearance of geometrical perturbations in the disk; it depends only on the model for the close binary system and its components, as well as the shapes of the light curves observed during superoutbursts.

Observations in one red band are not sufficient to reveal the physical nature of these perturbations, since red radiation is generated mainly in the outer parts of the disk, the common envelope, and the surface of the secondary, which is heated by the short-wavelength radiation of the boundary layer.

Let us consider how the hump shift was manifest in the orbital light curves during the observed superoutburst. We deleted measurements within $0.08P_{\rm orb}$ of the centers of eclipses. The deviations δR from the corresponding mean level for the remaining out-of-eclipse measurements were calculated to take into account the systematic drop in brightness as the brightness of the system was falling off.

Figure 9 shows δR as a function of the phase ϕ of the superhump period $P_{sh} = 0.060320^{\rm d}$. We used the ephemerides (2) to calculate ϕ. The different symbols denote observations made on different nights. The phase-dependent curve $\delta R(\phi)$ has a form characteristic of superhumps during the outburts. Since this figure shows the unaveraged data, it is possible to trace which observations (symbols) are related to which parts of the light curve. Since we know the calculated fluxes from the system components on the corresponding nights (Fig. 7), we can elucidate which parameters of the spiral-arm model give rise to the apparent superhump migration along the orbital light curve.

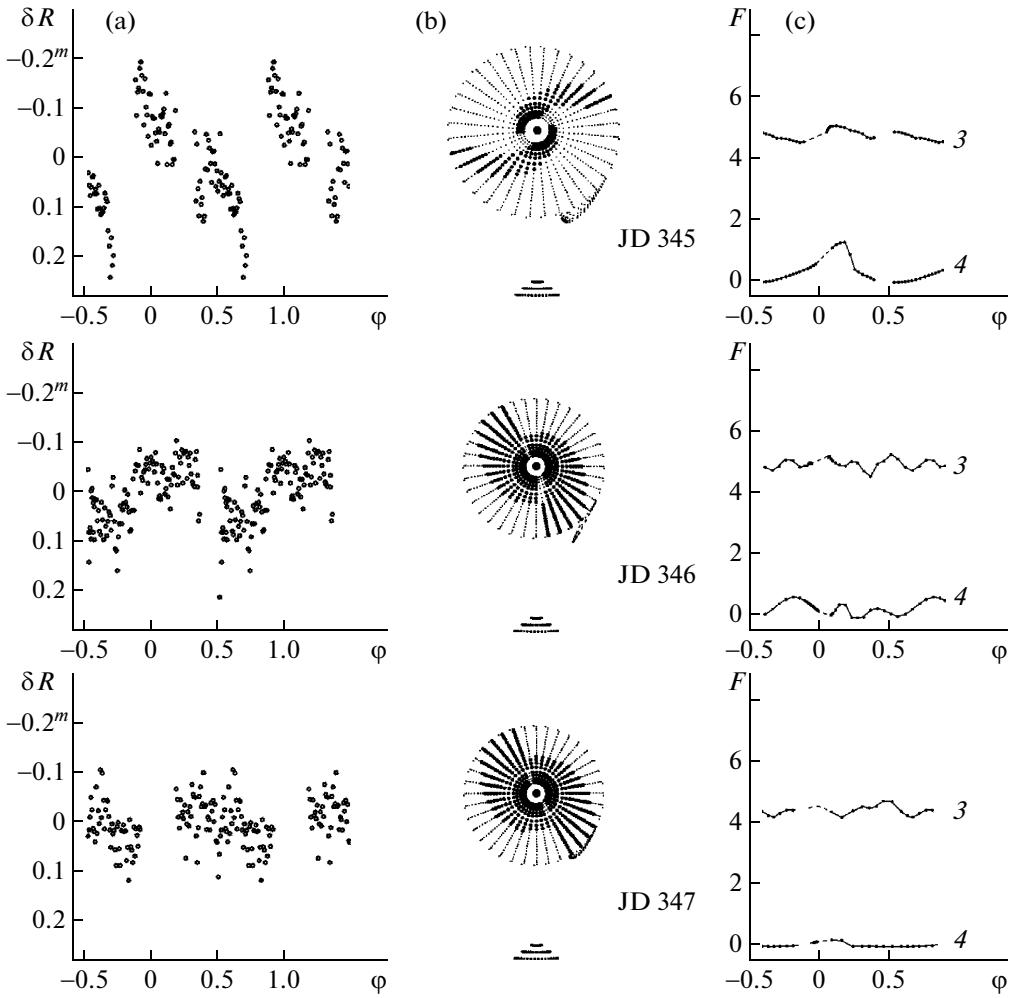

Fig. 11. Same as Fig. 10 for the observations obtained on May 28–30, 2010 (JD 2455345–JD 2455347).

Recall that our ΔR light curves have not only different out-of-eclipse maximum flux levels, but also different depths and orbital phases of the dips (Fig. 4), which vary from light curve to light curve. The accretion disk contributes most to the total R flux during the outburst, while the contributions of other other components, even the secondary, are at least a factor of three to five smaller (Fig. 7). The dependence of the disk radiation on the orbital phase, as well as the dip positions and depths, vary with the contribution from the spiral arms, which is superimposed on the relatively constant out-of-eclipse disk radiation. The maximum radiation from the disk at a phase φ occurs for the following spiral-arm orientation: (1) the spirals are symmetric and not very wide (or not too high, since the spiral width is a function of the spiral-crest height ζ in our code); (2) the inner slope of the more distant spiral arm with a pronounced reflection effect is clearly visible. Note that it is not possible to estimate what part of the UV radiation from the boundary layer on the outer slope of the nearest spiral arm is re-radiated in the red, since radiative transfer is not taken into account in the code.

Figures 10 and 11 show the superhump curves $\delta R(\phi)$ for light curves *2*–*7* (Figs. 10a and 11a). The orientation of the spiral arms on the accretion disk in the orbital plane for a given set is shown in the center; the contributions of the disk radiation (curve *3*) and hot line (curve *4*) are shown to the right (in arbitrary units). Here, the notation is the same as in Fig. 7. Some observations are absent from the light curves in Figs. 10a, 10c, 11a, and 11c; these observations were removed because they coincide with the primary minimum, $\Delta\varphi = (-0.08, +0.08)$. Apart from the smooth fall-off, the shape of the curves $F(\varphi)$ for the secondary (Fig. 7) is repeated from set to set, and these curves are not shown in Figs. 10c and 11c in order to avoid making them too cluttered.

In curves *2* and *5*, which are similar to each other, the maximum in the superhump curve $\delta R(\phi)$ with an

amplitude of $\sim 0.4^m$ arises due to the coincidence of the radiation maxima for the disk and the hot line at orbital phases $\varphi \sim 0.1$. The spiral arms near the outer part of the disk are localized at phases $\sim$0.7 and $\sim$0.2 (Figs. 10b and 11b); i.e., we observe the classical pattern obtained from eclipse mapping. The arrows in Fig. 10b indicate the orbital phase ranges where the contributions from spiral arms of the disk are maximum and minimum. The second maximum ($\varphi \sim 0.55$) in the curve of the disk radiation falls within the superhump minimum (Fig. 10a): the hot-line contribution is minimum here, and the contribution of the secondary (Fig. 7) has a local minimum due to the ellipsoidal effect.

For curve *3*, the solution obtained for our model yields fairly broad and asymmetric spiral arms. The maximum radiation from the accretion disk is observed at orbital phases $\varphi \sim 0.35$–0.8, due to the favorable conditions for observing the reflection effect at the inner slope of the spiral arm with its crest at $\varphi \sim 0.3$. The maximum flux from the secondary is also located here. The local minimum of the secondary flux is compensated by the local maximum of the disk contribution due to the ellipsoidal effect at phase $\varphi \sim 0.5$. In this set of observations, the sum of these two fluxes gives rise to a superhump with an amplitude of $\sim 0.35^m$ (Fig. 10a). The hot line contributes to the total flux only on the leeward side (analogous to a hot spot), but this contribution is not high: $F \sim 0.5$ units.

The orbital light curve obtained for the fourth set of observations (JD 2455344) has a classical form: there is a hump before the eclipse and weak oscillations of the out-of-eclipse brightness. The superhump amplitude (Fig. 10a) decreases to $\sim 0.25^m$; the superhump is mainly due to the flux from the leeward side of the hot line at phases $\varphi \sim 0.8$. The range of the oscillations of the accretion-disk flux over the orbital cycle is half that for the previous sets, and does not show any regular variations.

The superhump amplitude for curves *6* and *7*, does not exceed $\sim 0.2^m$ (Fig. 11a), and is comparable with the scatter of the points in the curves. This is clearly visible in curve *7*. The positions and amplitudes of the dips are determined by the complex, irregular variability of the spiral-arm radiation. The fluxes from the hot line and the secondary are small.

Thus, our results for the spiral-arm model lead us to conclude that the superhump flux is not directly associated with the orientation of the spiral arms, and is instead due to a combination of various factors.

The first and main factor is the increase in the flux from the windward side of the hot line. The spiral-arm orientation corresponds to the classical pattern obtained from eclipse mapping.

The second factor is associated with variations in the flux from the spiral arms of the disk during the orbital cycle due to changes in the visibility conditions for the inner slopes of the spiral arms, which are heated by the hot radiation from the boundary layer of the disk (the reflection effect on the disk).

The third factor is the amplitude of the reflection effect on the secondary. The contribution of this factor is appreciable only in the presence of high radiation fluxes from the inner disk regions, i.e., during the superoutburst maximum. It does not depend on the spiral-arm orientation relative to the secondary, but it helps increase the amplitude of the orbital variability of the out-of-eclipse brightness (and the superhump amplitude) under appropriate conditions; i.e., if a local increase in flux from the disk falls within orbital phases near $\varphi \sim 0.5$.

Let us now summarize our results.

1. We have used a spiral-arm model based on the generally accepted structure of a disk during a superoutburst: a non-circular disk is assumed to have spiral arms in its outer part, and a region of enhanced energy release exists near the hot line, i.e., the region where the gas flow interacts with the rotating disk.

2. Application of this model enabled us to reconstruct the shape, amplitude, and time-dependent behavior of the mean level of the out-of-eclipse brightness in the light curves of J0903 on the descending branch of the superoutburst with good accuracy,including dips with various depths and at various orbital phases.

3. To reconstruct the orbital phases and depths of the dips in the light curves, we must assume that the azimuths Φ of the spiral-arm crests near the outer edge of the disk can change. However, the assumption of regular changes in Φ contradicts gas-dynamical calculations that indicate that the spiral shocks appear due to the tidal effect of the secondary, which suggests that they should be at rest in a coordinate system rotating with the orbital period.

4. The dependence of the superhump orbital phase on Φ is not obvious. A superhump appears as a result of the summing of the fluxes of the spiral arms, the cycle-dependent flux from the hot line, and, to a smaller degree, the radiation from the secondary, whose surface is strongly heated by UV radiation from the inner regions of the disk. The origin of the observed regular variability in the flux from the hot line (from either the windward or leeward side) is not clear. The level of the flux from the windward side of the hot line is associated with the energy of the shock that arises due to the collision of matter of the rotating disk with the gaseous stream. The shock energy increases with increasing density and/or velocity of the disk material. One possibility is that a dense blob

of matter moves in the ring at the outer edge of the disk in accordance with Keplerian rotation. This blob moves more slowly than the main matter of the disk, and thus it will move in the opposite to the orbital motion in a rotating coordinate system. A similar hypothesis (injection of a blob of matter into the outer ring of the disk) was proposed in the 1980s [30] to explain the observed migration of a dip along the light curve of the low-massive X-ray binary HZ Her with the precessing accretion disk ($P_{\rm orb} = 1.70016772^{\rm d}$, $P_{pres} = 34.875^{\rm d}$ [52]). However, such blobs are unlikely to be able to exist for approximately 100 orbital cycles (the mean superoutburst duration).

5. All this implies that the model we have used to explain the superoutburst is not perfect. The observed rotation of the spiral-arm creasts could be due to a more complex structure of the accretion disk during the superoutburst, and may suggest that other factors must be taken into account.

An alternative model to explain superoutbursts and the nature of superhumps was proposed in [27]. This model assumes that a single spiral-density wave appears in the inner parts of the disk and precesses slowly around the compact star. However, this model likewise cannot answer some questions. In particular, the superhump light source in this model is a slowly precessing accretion region on the white dwarf near the orbital plane of the system. The geometrical size of this region is very small, and the maximum of its radiation is in the soft X-ray and UV. The flux in the optical and red is comprised of radiation from the outer, cooler parts of the disk ($T \leq 10\,000$ K) and the reduced UV flux that is absorbed by geometrical inhomogeneities of the disk and re-radiated at longer wavelengths. The schemes for matter flows in the inner parts of the disk [27, Fig. 1] do not indicate the presence of other geometrical inhomogeneities along the path of the superhump UV source, apart from the thickened outer edge of the accretion disk. Therefore, the proposed mechanism suggests that the superhump light source observed in the red can only be a "dynamical hot spot" that appears when the precessing UV flux from the accretion region is reprocessed by a directionally heated part of the disk. This "dynamical hot spot" can produce a superhump in the light curve, without invoking variable intensity of the hot line, the motion of tidal waves in the outer parts of the disk, complex interactions between the fluxes from the secondary and the disk, etc. However, it remains clear how this mechanism can explain the shift of the dips in orbital phase. Another unstudied phenomenon in this model is the observation of superhumps in the optical and red in close binaries with small orbital inclinations i: the superhump light source—the heated inner slope of the thickened edge of the disk covering a short range of azimuth—should be seen at all orbital phases in this model. The superhump amplitude should then decrease with decreasing i, which is not confirmed observationally.

9. CONCLUSIONS

The main results obtained in our study of the SU UMa dwarf nova J0903 during its superoutburst in May 2010 are as follows.

1. We have carried out photometric observations of the eruptive variable J0903 in the R filter of the Johnson photometric system (near-IR) during the superoutburst in May 2010 (JD 2455341−2455347). The observations cover an interval near the outburst maximum and the subsequent slow decrease in brightness in the second stage of the superoutburst.

2. The light curves convolved with orbital period (3) demonstrate qualitative changes in their shapes on the descending branch of the outburst. The amplitude of the light curve decreases smoothly from 0.8^m to 0.6^m over the course of six nights; the maximum brightness decreases from $\Delta R = 1.6^m$ near the maximum (May 25, 2010) to $\Delta R = 2.35^m$ six days later. All the J0903 light curves show deep dips in out-of-eclipse parts of the curves during the outburst; two orbital light curves have anomalous forms. Models taking into account geometrical perturbations on the surface of the accretion disk are required in order to reproduce the dips in the out-of-eclipse parts of the light curves. A hot-line model is required to fit the superhumps in the anomalous light curves at phases $\varphi \sim 0.1$−0.2 (i.e., during the egress from the primary minimum).

3. A spiral-arm model was used to determine the parameters of the accretion disk, hot line, and other components of J0903. Along with the hot line, the model includes geometrical inhomogeneities on the surface of the disk, namely, two thickenings of its outer edge that decrease exponentially in the vertical direction with approach toward the white dwarf and differ in azimuth by 160°−200°. We carried out fitting using this model in order to determine the parameters of J0903 for six parts of the superoutburst. The light curves synthesized with the obtained parameters fit the shapes of the observed curves and the dip characteristics (orbital phases and depths) well.

4. The accretion-disk radius in the red is $\sim 0.44a_0$ at the superoutburst maximum (it was $R_d \sim 0.28a_0$ before the outburst [10]) and the radial temperature distribution deviates from the canonical law with $\alpha_g = 0.75$ (α_g decreases to 0.647 near the maximum). The accretion-disk radius decreases smoothly to $\sim 0.33a_0$, the thickness of its outer edge decreases by a factor of two, and the temperature of the boundary layer approaches the temperature of the white dwarf as the superoutburst decays; α_g approaches its

canonical value, so that the balance between heating and cooling of the matter is restored.

5. Our computational results did not indicate the action of a single mechanism for the superhump phenomenon and the motion of the superhump in the rotating reference system. In the model we have used, the superhump appears due to the summing of the fluxes from the spiral arms and the cycle-dependent radiation of the hot line; the radiation from the secondary, whose surface is strongly heated by UV flux from the inner regions of the disk, contributes to a lesser degree. The origin of the long-periodic changes in the flux from the hot line is not clear.

6. The presence of spiral waves in the outer parts of the disk during the superoutburst is able formally reproduce the characteristics of the dips in the light curves, but only if the crests of the spiral arms located near the outer edge of the disk have time-dependent azimuths Φ. This contradicts the tidal character of the spiral waves in the outer parts of the disk. The dependences of the superhump, superhump amplitude, and other parameters of the spiral arms on the orbital phase Φ are not obvious, and the superhump characteristics are determined by other factors (see item 5). This suggests that different mechanisms are responsible for the appearance of the dips and the superhump.

ACKNOWLEDGMENTS

The authors thank V.G. Metlov for help in carrying out observations at the Crimean Laboratory of the Sternberg Astronomical Institute. This work was supported by the Russian Foundation for Basic Research (projects 09-02-00225, 11-02-00258), the Program of Support for Leading Scientific Schools of the Russian Federation (grant NSh-7179.2010.2), and the program "The Development of the Scientific Potential of Higher Education" (RNP 2.1.1.12706).

REFERENCES

1. B. Warner, *Cataclismic Variable Stars* (Cambridge Univ. Press, Cambridge, 1995).
2. H. C. Vogt, Astron. Astrophys. **36**, 369 (1974).
3. J. Papaloizou and J. E. Pringle, Astron. Astrophys. **70**, L65 (1978).
4. J. Papaloizou and J. E. Pringle, Mon. Not. R. Astron. Soc. **189**, 293 (1979).
5. H. C. Vogt, Astron. Astrophys. **88**, 66 (1980).
6. Y. Osaki, Astron. Astrophys. **144**, 369 (1985).
7. Y. Osaki, Publ. Astron. Soc. Pasif. **41**, 1005 (1989).
8. W. J. Duschl and M. Livio, Astron. Astrophys. **241**, 153 (1989).
9. P. Szkody, A. Henden, O. J. Fraser, et al., Astron. J. **129**, 2386 (2005).
10. S. P. Littlefair, V. S. Dhillon, T. R. Marsh, et al., Mon. Not. R. Astron. Soc. **388**, 1582 (2008).
11. *Catalina Real-time Transient Survey (CRTS)—Catalina Transients 20100522—CRTS Transient ID CSS100522:090351+330036—Current CRTS lightcurve*; http://nesssi.cacr.caltech.edu/catalina/20100522/100522132042412247 2p.html.
12. A. J. Drake, S. G. Djorgovski, A. Mahabal, et al., Astrophys. J. **696**, 870 (2009).
13. A. G. U. Agustino, vsnet-alert No. 11999 (2010).
14. T. Kato, vsnet-outburst No. 11262 (2010).
15. T. Kato, H. Maehara, M. Uemura, et al., Publ. Astron. Soc. Jpn. **62**, 1525 (2010).
16. N. Zacharias, D. G. Monet, S. E. Levine, et al., *Naval Observatory Merged Astrometric Dataset (NOMAD)*, VizieR On-line Data Catalog: I/297, http://cdsarc.u-strasbg.fr/viz-bin/Cat'I/29; Astron. Astrophys. Suppl. Ser. **205**, 4815Z (2004).
17. S. Roeser, E. Schilbach, H. Schwan, et al., Astron. Astrophys. **488**, 401 (2008).
18. S. P. Littlefair, V. S. Dhillon, T. R. Marsh, et al., Mon. Not. R. Astron. Soc. **381**, 827 (2007).
19. D. Kjurkchieva, D. Marchev, T. Khruzina, and G. Djurasevic, Astrophys. Space Sci. **306**, 217 (2006).
20. T. S. Khruzina, D. Kjurkchieva, D. Marchev, and G. Djurasevic, Astron. Rep. **51**, 318 (2007).
21. T. S. Khruzina, N. A. Katysheva, and S. Yu. Shugarov, Astron. Rep. **85**, 815 (2008).
22. D. Steeghs, in *Astrotomography, Indirect Imaging Methods in Observational Astronomy*, Ed. by H. M. J. Boffin, D. Steeghs, and J. Cuypers, Lect. Notes Phys. **573**, 45 (2001).
23. D. O'Donoghue, Mon. Not. R. Astron. Soc. **246**, 29 (1990).
24. D. Steeghs, E. T. Harlaftis, and K. Horne, Mon. Not. R. Astron. Soc. **290**, L28 (1997).
25. K. Sawada, T. Matsuda, and I. Hachisu, Mon. Not. R. Astron. Soc. **219**, 75 (1986).
26. E. T. Harlaftis and T. Marsh, Astron. Astrophys. **308**, 97 (1996).
27. D. V. Bisikalo, A. A. Boyarchuk, P. V. Kaigorodov, et al., Astron. Rep. **48**, 588 (2004).
28. I. Hachisu, M. Kato, and T. Kato, Astrophys. J. **606**, L139 (2004).
29. D. V. Bisikalo, P. V. Kaigorodov, A. A. Boyarchuk, and O. A. Kuznetsov, Astron. Rep. **49**, 701 (2005).
30. L. Crosa and P. E. Boynton, Astrophys. J. **235**, 999 (1980).
31. N. G. Bochkarev and E. A. Karitskaya, Astrophys. Space Sci. **154**, 189 (1989).
32. T. S. Khruzina, Astron. Rep. **45**, 255 (2001).
33. T. S. Khruzina, Astron. Rep. **49**, 783 (2005).
34. T. S. Khruzina, Astron. Rep. **44**, 446 (2000).
35. N. I. Shakura and R. A. Sunyaev, Astron. Astrophys. **24**, 337 (1973).
36. G. Djurasevic, Astrophys. Space Sci. **240**, 317 (1996).
37. T. S. Khruzina, A. M. Cherepashchuk, D. V. Bisikalo, et al., Astron. Rep. **47**, 214 (2003).
38. D. Himmelblau, *Applied Nonlinear Programming* (McGraw-Hill, New York, 1972; Mir, Moscow, 1975).

39. A. Udalski, Astron. J. **100**, 226 (1990).
40. R. Haefner, R. Schoembs, and N. Vogt, Astron. Astrophys. **77**, 7 (1979).
41. J. Patterson, Astron. J. **84**, 804 (1979).
42. V. Krzeminski and N. Vogt, Astron. Astrophys. **144**, 124 (1985).
43. K. O. Mason, in *The Physics of Accretion onto Compact Objects*, Ed. by K. P. Mason, M. G. Watson, and N. E. White, Lect. Notes Phys. **266**, 29 (1986).
44. T. Naylor, Mon. Not. R. Astron. Soc. **238**, 587 (1989).
45. R. Schoembs and N. Vogt, Astron. Astrophys. **91**, 25 (1980).
46. E. T. Harlaftis, B. J. M. Hassall, T. Naylor, et al., Mon. Not. R. Astron. Soc. **257**, 607 (1992).
47. I. Billington, T. R. Marsh, K. Horne, et al., Mon. Not. R. Astron. Soc. **279**, 1274 (1996).
48. B. Warner, D. O'Donoghue, and W. Wargau, Mon. Not. R. Astron. Soc. **238**, 73 (1989).
49. K. Horne, Nature **312**, 348 (1984).
50. B. Warner and D. O'Donoghue, Mon. Not. R. Astron. Soc. **233**, 705 (1988).
51. R. Whitehurst and A. King, Mon. Not. R. Astron. Soc. **249**, 25 (1991).
52. A. M. Cherepashchuk, N. A. Katysheva, T. S. Khruzina, and S. Yu. Shugarov, *Highly Evolved Close Binary Stars. Part I: Catalog* (Gordon and Breach Sci., Brussel, 1996).

Translated by N. Lipunova